

WUSH: Near-Optimal Adaptive Transforms for LLM Quantization

Jiale Chen JIALE.CHEN@IST.AC.AT *Institute of Science and Technology Austria (ISTA)*

Vage Egiazarian *Institute of Science and Technology Austria (ISTA)*

Roberto L. Castro *Red Hat AI*

Torsten Hoefler *ETH Zürich*

Dan Alistarh *Institute of Science and Technology Austria (ISTA) & Red Hat AI*

Abstract

Quantizing LLM weights and activations is a standard approach for efficient deployment, but a few extreme outliers can stretch the dynamic range and amplify low-bit quantization errors. Prior transform-based mitigations (e.g., Hadamard rotations) are fixed and data-agnostic, and their optimality for quantization has remained unclear. We derive closed-form optimal linear blockwise transforms for joint weight-activation quantization under standard RTN AbsMax-scaled block quantizers, covering both integer and floating-point formats. The resulting construction, WUSH, combines a Hadamard backbone with a data-dependent second-moment component to form a non-orthogonal transform that is provably near-optimal for FP and INT quantizers under mild assumptions while admitting an efficient fused GPU implementation. Empirically, WUSH improves W4A4 accuracy over the strongest Hadamard-based baselines (e.g., on Llama-3.1-8B-Instruct in MXFP4, it gains +2.8 average points with RTN and +0.7 with GPTQ) while delivering up to $6.6\times$ per-layer throughput over BF16 via FP4 MatMul. Source code is available at <https://github.com/IST-DASLab/WUSH>.

1 Introduction

Quantization of model weights (Dettmers et al., 2022; Frantar et al., 2023; Lin et al., 2024) or activations (Xiao et al., 2023; Ashkboos et al., 2024b) is now a standard tool for shrinking and accelerating large language models (LLMs) (Kurtic et al., 2025), making low-precision inference feasible on a wide range of hardware. A central difficulty, however, is that a few extreme “outlier” weights and activations expand the dynamic range and thereby degrade the effective resolution of low-bit representations.

One way to mitigate such outliers is to apply linear transforms before quantization (Jegou et al., 2008; Jégou et al., 2011); in the case of LLM quantization, this is often in the form of rotations that spread variance more evenly across channels (Chee et al., 2023; Tseng et al., 2024a; Ashkboos et al., 2024b; Liu et al., 2025). For LLMs, Hadamard rotations have been remarkably effective, and blockwise variants aligned with quantization groups have also been shown to be useful in practice. Egiazarian et al. (2025) recently showed that the blockwise Hadamard transform offers the best empirical performance for quantization among a large set of existing transforms. Yet, these transforms are typically fixed and data-agnostic: in

particular, the Hadamard transform does not adapt to the statistics of the underlying weights or activations. This raises a natural question: if the Hadamard transform is *not data-aware*, in what sense can it be considered optimal for quantization?

In this work, we address this question by deriving *closed-form optimal linear blockwise transforms* for joint weight-activation quantization, which are generally *non-orthogonal* and *adaptive*, i.e., data-aware. As opposed to prior methods such as SpinQuant (Liu et al., 2025) or FlatQuant (Sun et al., 2025), our approach is closed-form and calibration-based, as it does not require training or fine-tuning the entire model.

We call our construction *WUSH* and we show that it is optimal for floating-point (FP) block quantizers and asymptotically optimal for integer (INT) block quantizers. (The name WUSH is a mnemonic for its composition.) Consider a block of layer weights $\mathbf{W}_{(i)}$, with calibration activation $\mathbf{X}_{(i)}$. Then, the WUSH transform $\mathbf{T}_{\text{wush}(i)}$ is:

$$\mathbf{T}_{\text{wush}(i)} = \mathbf{H} \mathbf{S}_{(i)}^{-\frac{1}{2}} \mathbf{U}_{(i)}^\top \mathbf{W}_{(i)}^\top \quad (1)$$

where $\mathbf{W}'_{(i)}$ is the Cholesky decomposition of $\mathbf{W}_{(i)} \mathbf{W}_{(i)}^\top = \mathbf{W}'_{(i)} \mathbf{W}'_{(i)\top}$, the matrices $\mathbf{U}_{(i)}$, $\mathbf{S}_{(i)}$, $\mathbf{V}_{(i)}$ are from the singular value decomposition (SVD) of $\mathbf{W}'_{(i)\top} \mathbf{X}_{(i)} = \mathbf{U}_{(i)} \mathbf{S}_{(i)} \mathbf{V}_{(i)}^\top$, and \mathbf{H} is a Hadamard matrix. We define the transform more formally in Eq. (8).

Empirically, WUSH significantly improves end-to-end accuracy over prior transform-based baselines, nearly closing the gap between NVFP and MXFP formats, with consistent benefits when combined with GPTQ (Frantar et al., 2023). It improves W4A4 accuracy by up to +2.8 average points (MXFP4 RTN) and +0.7 points (MXFP4 GPTQ) over the Hadamard-based baseline on Llama-3.1-8B-Instruct. Despite using a distinct (data-aware) transform per block, WUSH admits an efficient fused GPU kernel whose throughput matches that of optimized blockwise Hadamard kernels while delivering up to $6.6\times$ per-layer speedups over BF16 due to the lower-precision (FP4) matrix multiplication.

2 Related Work

Post-training quantization (PTQ) and outliers. PTQ schemes, such as RTN (round-to-nearest), OBQ (Frantar & Alistarh, 2022), and GPTQ (Frantar et al., 2023), are sensitive to heavy-tailed outliers in the weights and activations of LLMs because a small number of extreme values can determine the quantization scale, leading to high error.

Non-uniform bitwidths and explicit outlier storage. One common strategy to mitigate outliers is to use non-uniform bitwidths. Methods such as LLM.int8() (Dettmers et al., 2022), SpQR (Dettmers et al., 2024), and QUIK (Ashkboos et al., 2024a) explicitly separate and store outliers in higher precision, while HPTQ (Chen et al., 2025) uses Huffman encoding to compress the outliers and reduce their storage costs. These approaches can achieve high accuracy at a low effective bitwidth, however, the resulting formats are irregular and require specialized kernels.

Transform-based outlier mitigation. Another line of work applies transforms to the weights and activations before quantization to reduce the impact of outliers. SmoothQuant

(Xiao et al., 2023) and AWQ (Lin et al., 2024) rescale channels to stabilize the dynamic ranges of weights and activations. QuIP (Chee et al., 2023) introduces an incoherence processing step. QuIP# (Tseng et al., 2024a), QTIP (Tseng et al., 2024b), and QuaRot (Ashkboos et al., 2024b) use Hadamard transforms to spread outlier energy across channel dimensions, while SpinQuant (Liu et al., 2025) and FlatQuant (Sun et al., 2025) learn transforms optimized on calibration data. However, their transforms are heuristic and costly to learn, which limits their accuracy or practicality when applied to fast, per-token activation quantization in large models.

Blockwise transforms and emerging FP formats. The recent FP formats, such as MXFP (MX Alliance, 2023) and NVFP (NVIDIA, 2024), have motivated blockwise transform schemes. Shao et al. (2025) indicates that blockwise Hadamard transforms can be more effective under these FP formats than full-layer transforms, but Egiazarian et al. (2025) highlights the limited gains achievable with Hadamard alone, linking this to the properties of the underlying weight and activation distributions. In contrast, this work (WUSH) derives a closed-form, data-aware optimal blockwise transform and analyzes how such a transform interacts with both FP and INT block quantizers.

3 Methodology

Problem setup. We formulate the transformed weight-activation quantization problem as follows. Define $\mathbf{W} \in \mathbb{R}^{d_{\text{in}} \times d_{\text{out}}}$ as the weight of a linear layer with d_{in} input channels and d_{out} output channels. Define $\mathbf{X} \in \mathbb{R}^{d_{\text{in}} \times d_{\text{batch}}}$ as the calibration input activation with d_{in} embedding channels and d_{batch} tokens. Define $q(\cdot)$ as a quantizer that maps a matrix of continuous values to quantized values (we will specify q later). Let $\mathbf{T}_W, \mathbf{T}_X \in \mathbb{R}^{d_{\text{in}} \times d_{\text{in}}}$ be the transforms applied to \mathbf{W} and \mathbf{X} , respectively. For weight-activation quantization, the output activation $\mathbf{W}^\top \mathbf{X}$ becomes $q(\mathbf{T}_W \mathbf{W})^\top q(\mathbf{T}_X \mathbf{X})$. Our goal is to choose \mathbf{T}_W and \mathbf{T}_X such that the L_2 output loss

$$\ell = d_{\text{out}}^{-1} d_{\text{batch}}^{-1} \left\| q(\mathbf{T}_W \mathbf{W})^\top q(\mathbf{T}_X \mathbf{X}) - \mathbf{W}^\top \mathbf{X} \right\|_F^2 \quad (2)$$

is minimized under the given quantizer q . The constant $d_{\text{out}}^{-1} d_{\text{batch}}^{-1}$ is added to simplify the analysis later.

Block-independent constraint. While the weights can be pre-quantized, the activations must be transformed and quantized dynamically at inference time. To reduce the computational overhead of these operations, it is common (Egiazarian et al., 2025) to constrain $\mathbf{T}_W, \mathbf{T}_X$ to be block-diagonal transforms, and q to be an RTN (round-to-nearest) quantizer with AbsMax (the maximum absolute value within a group) scales. We assume that the quantization is applied to each sub-column vector of shape $d \times 1$ and that the transform block size aligns with the quantization group size d , with d being a factor of d_{in} and a power

of 2. Denote the block partitions of the matrices as

$$\begin{aligned}
\mathbf{T}_W &= \text{diag} \left(\mathbf{T}_{W_{(1)}}, \dots, \mathbf{T}_{W_{(d_{\text{in}}/d)}} \right), & \mathbf{T}_{W_{(i)}} &\in \mathbb{R}^{d \times d}, \\
\mathbf{T}_X &= \text{diag} \left(\mathbf{T}_{X_{(1)}}, \dots, \mathbf{T}_{X_{(d_{\text{in}}/d)}} \right), & \mathbf{T}_{X_{(i)}} &\in \mathbb{R}^{d \times d}, \\
\mathbf{W}^\top &= \left[\mathbf{W}_{(1)}^\top, \dots, \mathbf{W}_{(d_{\text{in}}/d)}^\top \right], & \mathbf{W}_{(i)} &\in \mathbb{R}^{d \times d_{\text{out}}}, \\
\mathbf{X}^\top &= \left[\mathbf{X}_{(1)}^\top, \dots, \mathbf{X}_{(d_{\text{in}}/d)}^\top \right], & \mathbf{X}_{(i)} &\in \mathbb{R}^{d \times d_{\text{batch}}}.
\end{aligned} \tag{3}$$

Then, we can express the output without and with weight-activation quantization, respectively, as

$$\begin{aligned}
\mathbf{W}^\top \mathbf{X} &= \sum_{i=1}^{d_{\text{in}}/d} \mathbf{W}_{(i)}^\top \mathbf{X}_{(i)}, \\
q(\mathbf{T}_W \mathbf{W})^\top q(\mathbf{T}_X \mathbf{X}) &= \sum_{i=1}^{d_{\text{in}}/d} q \left(\mathbf{T}_{W_{(i)}} \mathbf{W}_{(i)} \right)^\top q \left(\mathbf{T}_{X_{(i)}} \mathbf{X}_{(i)} \right).
\end{aligned} \tag{4}$$

Finally, define the (normalized) blockwise output loss as

$$\ell_{(i)} = d_{\text{out}}^{-1} d_{\text{batch}}^{-1} \left\| q \left(\mathbf{T}_{W_{(i)}} \mathbf{W}_{(i)} \right)^\top q \left(\mathbf{T}_{X_{(i)}} \mathbf{X}_{(i)} \right) - \mathbf{W}_{(i)}^\top \mathbf{X}_{(i)} \right\|_{\text{F}}^2. \tag{5}$$

We will approximate the layerwise loss as $\ell \approx \sum_{i=1}^{d_{\text{in}}/d} \ell_{(i)}$ and minimize the blockwise losses $\ell_{(i)}$ independently.

Optimal block-diagonal transforms. In the following, we will prove, under reasonable assumptions, that there exist closed-form optimal transforms for each block. These transforms are provably optimal for FP and asymptotically optimal for INT quantization. Let $\mathbf{W}'_{(i)}, \mathbf{X}'_{(i)} \in \mathbb{R}^{d \times d}$ be matrices that satisfy

$$\begin{aligned}
\mathbf{W}'_{(i)} \mathbf{W}'_{(i)}^\top &= d_{\text{out}}^{-1} \mathbf{W}_{(i)} \mathbf{W}_{(i)}^\top, \\
\mathbf{X}'_{(i)} \mathbf{X}'_{(i)}^\top &= d_{\text{batch}}^{-1} \mathbf{X}_{(i)} \mathbf{X}_{(i)}^\top,
\end{aligned} \tag{6}$$

respectively. Without loss of generality (Appendix Section A.1), we let \mathbf{W}' and \mathbf{X}' be the lower triangular matrices from the Cholesky decomposition of the second moments $d_{\text{out}}^{-1} \mathbf{W}_{(i)} \mathbf{W}_{(i)}^\top$ and $d_{\text{batch}}^{-1} \mathbf{X}_{(i)} \mathbf{X}_{(i)}^\top$. In the case of $\text{rank}(\mathbf{W}_{(i)}) < d$ or $\text{rank}(\mathbf{X}_{(i)}) < d$, we can dampen the diagonal of the second moments before the Cholesky decomposition. Let the orthogonal matrices $\mathbf{U}_{(i)}, \mathbf{V}_{(i)} \in \mathbb{R}^{d \times d}$ and the diagonal matrix $\mathbf{S}_{(i)} \in \mathbb{R}^{d \times d}$ be the singular value decomposition (SVD) of

$$\mathbf{W}'_{(i)} \mathbf{X}'_{(i)}^\top = \mathbf{U}_{(i)} \mathbf{S}_{(i)} \mathbf{V}_{(i)}^\top. \tag{7}$$

Let $\mathbf{H} \in \{\pm d^{-\frac{1}{2}}\}^{d \times d}$ be a normalized (orthogonal) Hadamard matrix. Then, we will show that the optimal $\mathbf{T}_{W_{(i)}}$ and $\mathbf{T}_{X_{(i)}}$ can be constructed as

$$\begin{aligned}
\mathbf{T}_{\text{xvsh}(i)} &= \mathbf{H} \mathbf{S}_{(i)}^{-\frac{1}{2}} \mathbf{V}_{(i)}^\top \mathbf{X}'_{(i)}^\top, \\
\mathbf{T}_{\text{wush}(i)} &= \mathbf{H} \mathbf{S}_{(i)}^{-\frac{1}{2}} \mathbf{U}_{(i)}^\top \mathbf{W}'_{(i)}^\top,
\end{aligned} \tag{8}$$

respectively. Note that¹

$$\mathbf{T}_{\text{xvsh}(i)} = \mathbf{T}_{\text{wush}(i)}^{-\top}, \quad (9)$$

which can be easily verified by calculating $\mathbf{T}_{\text{xvsh}(i)}\mathbf{T}_{\text{wush}(i)}^\top = \mathbf{I}$, where \mathbf{I} is the identity matrix.

Remark. The Hadamard matrix \mathbf{H} is the only data-agnostic ingredient in our optimal formulation in Eq. (8). Incidentally, this explains why it has been empirically observed to be an effective data-agnostic orthogonal transform.

Algorithm 1: Compute WUSH and Pre-Quantize Weights

Input:

weights $\mathbf{W} \in \mathbb{R}^{d_{\text{in}} \times d_{\text{out}}}$, activations $\mathbf{X} \in \mathbb{R}^{d_{\text{in}} \times d_{\text{batch}}}$, Hadamard $\mathbf{H} \in \{\pm d^{-\frac{1}{2}}\}^{d \times d}$, damping ratio $\lambda \in \mathbb{R}_{\geq 0}$, flag *flag* of whether to quantize with GPTQ

Output:

WUSH transform $\mathbf{T}_{\text{wush}(i)} \in \mathbb{R}^{d \times d}$ and pre-quantized weight $\tilde{\mathbf{W}}_{(i)} \in \mathbb{R}^{d \times d_{\text{out}}}$ for each block $i = 1, \dots, d_{\text{in}}/d$

- 1: $\mathcal{H} \leftarrow d_{\text{batch}}^{-1} \mathbf{X} \mathbf{X}^\top + \lambda \mathbf{I}$ ▷ same as GPTQ’s Hessian
 - 2: $\mathbf{X}' \mathbf{X}'^\top \leftarrow \text{Cholesky}(\mathcal{H})$ ▷ lower triangular $\mathbf{X}' \in \mathbb{R}^{d_{\text{in}} \times d_{\text{in}}}$
 - 3: $\mathbf{Y} \leftarrow \mathbf{W}^\top \mathbf{X}'$ ▷ target output $\mathbf{Y} \in \mathbb{R}^{d_{\text{out}} \times d_{\text{in}}}$
 - 4: **for** $i \leftarrow d_{\text{in}}/d$ **to** 1 **do**
 - 5: $j_1, j_2 \leftarrow (i - 1)d + 1, id$ ▷ row/column selection indices
 - 6: $\mathbf{U} \mathbf{S} \mathbf{V}^\top \leftarrow \text{SVD}(\mathbf{Y}[1 : d_{\text{out}}, j_1 : j_2])$ ▷ $\mathbf{U} \in \mathbb{R}^{d_{\text{out}} \times d}$, $\mathbf{S} \in \mathbb{R}^{d \times d}$, $\mathbf{V} \in \mathbb{R}^{d \times d}$
 - 7: $\mathbf{U}, \mathbf{S} \leftarrow d_{\text{out}}^{\frac{1}{2}} \mathbf{U}, d_{\text{out}}^{-\frac{1}{2}} \mathbf{S}$ ▷ normalize by output dimensions
 - 8: $\mathbf{T}_{\text{wush}(i)} \leftarrow \mathbf{H} \mathbf{S}^{\frac{1}{2}} \mathbf{V}^\top (\mathbf{X}'[j_1 : j_2, j_1 : j_2])^{-1}$ ▷ $\mathbf{T}_{\text{wush}(i)} = \mathbf{T}_{\text{xvsh}(i)}^{-\top} \in \mathbb{R}^{d \times d}$
 - 9: $\tilde{\mathbf{W}} \leftarrow \mathbf{H} \mathbf{S}^{\frac{1}{2}} \mathbf{U}^\top$ ▷ transformed weights $\tilde{\mathbf{W}} \in \mathbb{R}^{d \times d_{\text{out}}}$
 - 10: **if** *flag* **then**
 - 11: $\tilde{\mathbf{W}}_{(i)} \leftarrow \text{GPTQ}(\text{weight} = \tilde{\mathbf{W}}, \text{Hessian} = \mathbf{H} \mathbf{S} \mathbf{H}^\top)$ ▷ GPTQ subroutine (intra-block GPTQ error propagation)
 - 12: $\mathbf{Y} \leftarrow \mathbf{Y} - \tilde{\mathbf{W}}_{(i)}^\top \mathbf{T}_{\text{wush}(i)} \mathbf{X}'[j_1 : j_2, 1 : d_{\text{in}}]$ ▷ inter-block GPTQ error propagation
 - 13: **else**
 - 14: $\tilde{\mathbf{W}}_{(i)} \leftarrow q(\tilde{\mathbf{W}})$ ▷ RTN (round-to-nearest) fallback
 - 15: $\mathbf{Y} \leftarrow \mathbf{Y} - \tilde{\mathbf{W}}_{(i)}^\top \mathbf{T}_{\text{wush}(i)} \mathbf{X}'[j_1 : j_2, 1 : d_{\text{in}}]$ ▷ blockwise triangular solve
 - 16: **end if**
 - 17: **end for**
-

GPTQ integration. In practice, the second-order information $d_{\text{batch}}^{-1} \mathbf{X}_{(i)} \mathbf{X}_{(i)}^\top$ in Eq. (6) can be obtained either from the calibration activations or from the Hessian matrix; the latter coincides, up to a constant factor, with the Hessian used in GPTQ. Therefore, it is a natural idea to integrate WUSH into GPTQ. However, GPTQ updates the weights iteratively via error propagation, while the WUSH transform is constructed from the second-order statistics of the updated weights. This coupling between weight updates and transform construction requires an interleaved computational schedule. Algorithm 1 summarizes the procedure used

1. The $-\top$ superscript means $(\cdot)^{-\top} = ((\cdot)^{-1})^\top = ((\cdot)^\top)^{-1}$.

to compute the blockwise² WUSH transforms and pre-quantized weights for a linear layer, using either GPTQ or RTN. The GPTQ error propagations are decomposed into intra-block and inter-block updates similar to its original paper (Frantar et al., 2023). For the intra-block updates, we apply the standard GPTQ subroutine to the current transformed weight block using the corresponding transformed Hessian. For inter-block propagation, we follow GPTQ’s usual blockwise updates, but we implement them using the equivalent formulation from Chen et al. (2025), which simplifies the procedure by avoiding explicit Hessian inversion. The model-level calibration pipeline closely follows that of GPTQ: layers are processed sequentially, and after processing a layer, the calibration activations are propagated through the quantized layer to provide the inputs for calibrating the next one. During inference, the forward pass of a linear layer is calculated as

$$\sum_{i=1}^{d_{\text{in}}/d} \tilde{\mathbf{W}}_{(i)}^\top q\left(\mathbf{T}_{\text{wush}(i)} \tilde{\mathbf{X}}_{(i)}\right) \quad (10)$$

with $\tilde{\mathbf{W}}_{(i)} \in \mathbb{R}^{d \times d_{\text{out}}}$ being the pre-quantized and transformed weight blocks and $\tilde{\mathbf{X}}_{(i)} \in \mathbb{R}^{d \times d_{\text{batch}}}$ being the new activation blocks instead of the calibration ones.

4 Theoretical Derivation

In this section, we focus on the question of finding optimal transforms that minimize the loss of one block $\ell_{(i)}$ in Eq. (5). To build intuition for the proof, Figure 1 visualizes how different transforms reshape the expected quantization error under FP and INT block quantizers, in a 2D toy setting. Throughout, we omit the block subscript (i) to simplify notation. Also, the detailed derivation steps of some equations are deferred to Appendix Section A.3.

4.1 Problem Setup and General Proof Approach

Probabilistic reformulation. We reformulate the problem from a probabilistic perspective. We split the matrices $\mathbf{W} = [\mathbf{w}_1, \dots, \mathbf{w}_{d_{\text{out}}}]$ and $\mathbf{X} = [\mathbf{x}_1, \dots, \mathbf{x}_{d_{\text{batch}}}]$ into columns $\mathbf{w}_k, \mathbf{x}_k \in \mathbb{R}^d$ and treat the columns as i.i.d. samples from d -dimensional independent distributions $\mathbf{w} \sim \mathcal{D}_{\mathbf{w}}$ and $\mathbf{x} \sim \mathcal{D}_{\mathbf{x}}$, respectively. We motivate this multivariate modeling choice in Appendix Section A.2. We can reinterpret the blockwise loss in Eq. (5) as

$$\ell = \mathbb{E}_{\mathbf{w}, \mathbf{x}} \left(q\left(\mathbf{T}_{\mathbf{W}} \mathbf{w}\right)^\top q\left(\mathbf{T}_{\mathbf{X}} \mathbf{x}\right) - \mathbf{w}^\top \mathbf{x} \right)^2. \quad (11)$$

Similarly, we can also reinterpret Eq. (6) so that the matrices \mathbf{W}' and \mathbf{X}' satisfy

$$\begin{aligned} \mathbf{W}' \mathbf{W}'^\top &= \mathbb{E}_{\mathbf{w}} \mathbf{w} \mathbf{w}^\top, \\ \mathbf{X}' \mathbf{X}'^\top &= \mathbb{E}_{\mathbf{x}} \mathbf{x} \mathbf{x}^\top, \end{aligned} \quad (12)$$

respectively.

2. The $\dots[a : b, c : d]$ notation in algorithm selects block with row indices from a to b and column indices from c to d , all inclusive.

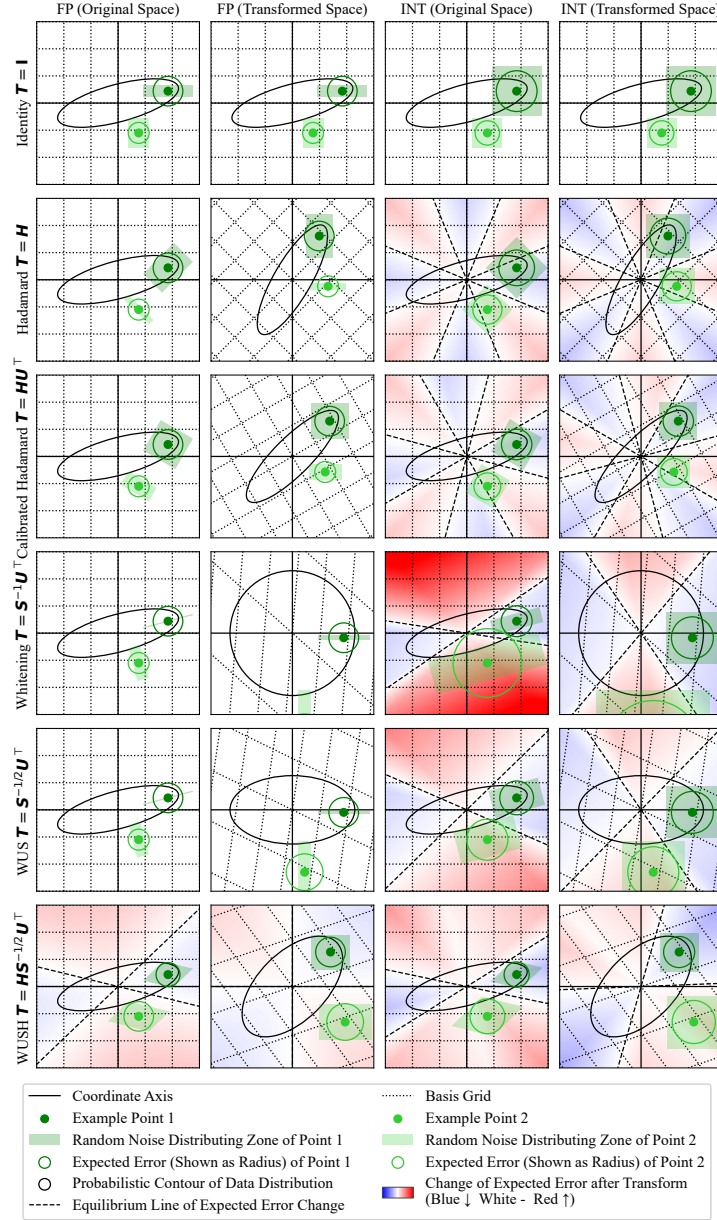


Figure 1: **2D illustration of how transforms shape the one-sided quantization error $\|T^{-1}\varepsilon(T\mathbf{y})\|^2$ in Eq. (14) under FP and INT block quantizers.** Each row corresponds to a different transform T (identity; Hadamard: 45° rotation; calibrated Hadamard: equally spreading energy into each dimension; whitening; WUS: WUSH without Hadamard; WUSH), and columns show FP and INT quantization in both original and transformed space. The dotted grid shows the basis induced by the transform. Two example points are shown in detail with their induced quantization noise support (Sections 4.2.1 and 4.3.1) represented as shaded parallelograms, and the corresponding average (expected) error magnitude (Eq. (14)) represented as the radii of circles (not necessarily proportional to the area of parallelograms). For each point on the plane, we visualize its expected error change (compared to that of the identity transform) calculated in the original space, with blue/red background heatmaps indicating lower/higher and dashed lines indicating the equilibrium set where the expected error is unchanged. No transform can reduce the error for all points on the plane, otherwise we would be able to repeatedly apply that transform until the error reaches zero. Thus, the key idea is to reduce the error around typical data distributions. The black ellipse depicts a representative data distribution contour. Overall, WUSH more effectively reduces the error by aligning the ellipse’s major axis to the error reduction (blue) regions.

Unbiased quantization. We assume that q is a stochastic and unbiased quantizer, i.e., for a vector $\boldsymbol{\alpha} \in \mathbb{R}^d$, the quantization error $\varepsilon(\boldsymbol{\alpha}) = q(\boldsymbol{\alpha}) - \boldsymbol{\alpha}$ is a random vector with $\mathbb{E}_{\varepsilon(\boldsymbol{\alpha})} \varepsilon(\boldsymbol{\alpha}) = \mathbf{0}$. We further constrain $\mathbf{T}_W = \mathbf{T}_X^{-\top}$ such that $q(\mathbf{T}_W \mathbf{w})^\top q(\mathbf{T}_X \mathbf{x})$ is unbiased with respect to $\mathbf{w}^\top \mathbf{x}$. Then, using the first-order approximation, we can split ℓ in Eq. (11) into two non-negative terms:

$$\ell = \left(\mathbb{E}_{\mathbf{w}, \varepsilon(\mathbf{T}_W \mathbf{w})} \left\| \mathbf{X}'^\top \mathbf{T}_W^{-1} \varepsilon(\mathbf{T}_W \mathbf{w}) \right\|^2 \right) + \left(\mathbb{E}_{\mathbf{x}, \varepsilon(\mathbf{T}_X \mathbf{x})} \left\| \mathbf{W}'^\top \mathbf{T}_X^{-1} \varepsilon(\mathbf{T}_X \mathbf{x}) \right\|^2 \right). \quad (13)$$

The detailed derivation is given in Appendix Eq. (37).

Problem reduction. We can compute the optimal \mathbf{T}_W and \mathbf{T}_X individually for each of the non-negative terms and verify that $\mathbf{T}_W = \mathbf{T}_X^{-\top}$. The two terms have similar forms and can be optimized in similar ways. We focus on finding the optimal \mathbf{T}_X for the second term. Define the d -dimensional random variable $\mathbf{y} = \mathbf{W}'^\top \mathbf{x}$ and denote its distribution as $\mathbf{y} \sim \mathcal{D}_y$. Define the transformation matrix $\mathbf{T} = \mathbf{T}_X \mathbf{W}'^{-\top}$. Then, the second term in Eq. (13) becomes

$$\begin{aligned} \mathbb{E}_{\mathbf{x}, \varepsilon(\mathbf{T}_X \mathbf{x})} \left\| \mathbf{W}'^\top \mathbf{T}_X^{-1} \varepsilon(\mathbf{T}_X \mathbf{x}) \right\|^2 &= \mathbb{E}_{\mathbf{x}, \varepsilon(\mathbf{T}_X \mathbf{x})} \left\| \left(\mathbf{T}_X \mathbf{W}'^{-\top} \right)^{-1} \varepsilon \left(\mathbf{T}_X \left(\mathbf{W}'^{-\top} \mathbf{y} \right) \right) \right\|^2 \\ &= \mathbb{E}_{\mathbf{y}, \varepsilon(\mathbf{T} \mathbf{y})} \left\| \mathbf{T}^{-1} \varepsilon(\mathbf{T} \mathbf{y}) \right\|^2 \end{aligned} \quad (14)$$

Therefore, the two-sided quantization problem in Eq. (11) is reduced to finding the optimal $\mathbf{T} \in \mathbb{R}^{d \times d}$ that minimizes the one-sided quantization loss $\mathbb{E}_{\mathbf{y}, \varepsilon(\mathbf{T} \mathbf{y})} \left\| \mathbf{T}^{-1} \varepsilon(\mathbf{T} \mathbf{y}) \right\|^2$ and compute

$$\mathbf{T}_X = \mathbf{T} \mathbf{W}'^\top. \quad (15)$$

Transformation parameterization. Let the unknown orthogonal matrices $\mathbf{U}', \mathbf{R} \in \mathbb{R}^{d \times d}$ and the unknown diagonal matrix $\mathbf{S}' \in \mathbb{R}^{d \times d}$ be the singular value decomposition (SVD) of $\mathbf{T} \mathbf{U} \mathbf{S} = \mathbf{U}' \mathbf{S}' \mathbf{R}^\top$ with \mathbf{U}, \mathbf{S} defined in Eq. (7); thus, \mathbf{T} can be parameterized as

$$\mathbf{T} = \mathbf{U}' \mathbf{S}' \mathbf{R}^\top \mathbf{S}^{-1} \mathbf{U}^\top. \quad (16)$$

Denote $\mathbf{S} = \text{diag}(s_1, \dots, s_d)$ and $\mathbf{S}' = \text{diag}(s'_1, \dots, s'_d)$. Without loss of generality, assume $s_1 \geq \dots \geq s_d > 0$ and $s'_1 \geq \dots \geq s'_d > 0$. A useful property of \mathbf{S} is

$$\text{tr}(\mathbf{S}^2) \geq d^{-1} (\text{tr}(\mathbf{S}))^2 \geq d^{-1} \text{tr}(\mathbf{S}^2) \quad (17)$$

with detailed steps in Eq. (38). The equality $\text{tr}(\mathbf{S}^2) = d^{-1} (\text{tr}(\mathbf{S}))^2$ is attained when all s_i are the same (all singular values are inliers). The equality $d^{-1} (\text{tr}(\mathbf{S}))^2 = d^{-1} \text{tr}(\mathbf{S}^2)$ is attained when $\text{tr}(\mathbf{S}) \rightarrow s_1$ (a singular value is an extreme outlier).

Theorem 1 (Optimal Transform) *The optimal configuration of \mathbf{T} for floating-point (FP) data types is $\mathbf{U}' = \mathbf{H}$, $\mathbf{S}' = \mathbf{S}^{\frac{1}{2}}$, and $\mathbf{R} = \mathbf{I}$. For integer (INT) types, the same configuration is optimal up to a $d^{o(1)}$ factor for zero-mean multivariate Gaussian/Laplacian distributed data and within a d factor for any distribution.*

Proof We provide detailed proofs for FP and INT in Sections 4.2 and 4.3, respectively. For each data type, we apply a two-step proof strategy. We first (Sections 4.2.1 and 4.3.1) provide a smooth modeling of the quantizer and treat the type casting errors as random noise. Secondly (Sections 4.2.2 and 4.3.2), we calculate the expected quantization error, Eq. (14), with respect to the parameterized transform, Eq. (16), and minimize this expectation by solving the corresponding optimization problem. ■

The optimal \mathbf{T}_X , aka the WUSH construction \mathbf{T}_{wush} in Eq. (8), is obtained by applying Theorem 1 and Eqs. (15), (16).

4.2 Proof for Floating-Point (FP) Types

4.2.1 QUANTIZATION ERROR MODELING

For a number in FP types, the quantization error tends to be proportional to its absolute value. Formally, for a vector $\boldsymbol{\alpha} \in \mathbb{R}^d$, we can model the quantization error as

$$\varepsilon(\boldsymbol{\alpha}) = \text{diag}(\boldsymbol{\eta}) \boldsymbol{\alpha} \quad (18)$$

where $\boldsymbol{\eta} = [\eta_1, \dots, \eta_d]^\top \in \mathbb{R}^d$ is a random vector of i.i.d. samples from the distribution $\eta \sim \mathcal{D}_\eta$ with $\mathbb{E}_\eta \eta = 0$. We provide more rigorous justifications for why this modeling makes sense in Appendix Section A.4.2.

4.2.2 LOSS MINIMIZATION

Using the quantization error modeling in Eq. (18), the minimization objective in Eq. (14) becomes

$$\mathbb{E}_{\mathbf{y}, \varepsilon(\mathbf{T}\mathbf{y})} \|\mathbf{T}^{-1} \varepsilon(\mathbf{T}\mathbf{y})\|^2 = (\mathbb{E}_\eta \eta^2) \text{tr} \left(\mathbf{T}^{-1} \left(\left(\mathbf{U}' \mathbf{S}'^2 \mathbf{U}'^\top \right) \odot \mathbf{I} \right) \mathbf{T}^{-\top} \right) \quad (19)$$

with \odot representing elementwise multiplication, and with detailed steps in Eq. (39). The lower bound of the trace term in Eq. (19) is

$$\text{tr} \left(\mathbf{T}^{-1} \left(\left(\mathbf{U}' \mathbf{S}'^2 \mathbf{U}'^\top \right) \odot \mathbf{I} \right) \mathbf{T}^{-\top} \right) \geq d^{-1} (\text{tr}(\mathbf{S}))^2 \quad (20)$$

and the equality can be attained by choosing $\mathbf{U}' = \mathbf{H}$, $\mathbf{S}' = \mathbf{S}^{\frac{1}{2}}$, and $\mathbf{R} = \mathbf{I}$, with detailed steps in Eqs. (40), (41).

4.2.3 DISCUSSION

Under our smooth modeling in Eq. (18), for any orthogonal \mathbf{T} (including the identity $\mathbf{T} = \mathbf{I}$ and the Hadamard $\mathbf{T} = \mathbf{H}$), the minimization objective becomes trivially

$$\mathbb{E}_{\mathbf{y}, \varepsilon(\mathbf{T}\mathbf{y})} \|\mathbf{T}^{-1} \varepsilon(\mathbf{T}\mathbf{y})\|^2 = (\mathbb{E}_\eta \eta^2) \text{tr}(\mathbf{S}^2) \quad (21)$$

with detailed steps in Eq. (42). Thus, orthogonal transforms will not be helpful for reducing the quantization error. Comparing the trace terms in Eqs. (20), (21) using the inequality

Eq. (17), the WUSH transform can reduce the error by at most d times in the extreme outlier scenario. Also note that the non-trivial choices $\mathbf{U}' = \mathbf{H}$ and $\mathbf{S}' = \mathbf{S}^{\frac{1}{2}}$ are both essential for reducing the error. Either trivial choices of $\mathbf{U}' = \mathbf{I}$ or $\mathbf{S}' = \mathbf{I}$ will lead to the same suboptimal trace term

$$\text{tr} \left(\mathbf{T}^{-1} \left(\left(\mathbf{U}' \mathbf{S}'^2 \mathbf{U}'^\top \right) \odot \mathbf{I} \right) \mathbf{T}^{-\top} \right) = \text{tr} (\mathbf{S}^2) \quad (22)$$

as that in the case of the orthogonal \mathbf{T} in Eq. (21), with detailed steps in Eqs. (43), (44). Figure 1 (left two columns) also visualizes these results.

4.3 Proof for Integer (INT) Data Types

4.3.1 QUANTIZATION ERROR MODELING

For a number in INT types, the quantization error tends to be proportional to the maximum absolute value within a quantization group. Formally, for a vector $\boldsymbol{\alpha} \in \mathbb{R}^d$, we can model the quantization error as

$$\varepsilon(\boldsymbol{\alpha}) = \|\boldsymbol{\alpha}\|_\infty \boldsymbol{\eta} \quad (23)$$

where $\boldsymbol{\eta} = [\eta_1, \dots, \eta_d]^\top \in \mathbb{R}^d$ is a random vector of i.i.d. samples from the distribution $\eta \sim \mathcal{D}_\eta$ with $\mathbb{E}_\eta \eta = 0$. We provide more rigorous justifications for why this modeling makes sense in Appendix Section A.4.1.

4.3.2 LOSS MINIMIZATION

Using the quantization error modeling in Eq. (23), the minimization objective in Eq. (14) becomes

$$\mathbb{E}_{\mathbf{y}, \varepsilon(\mathbf{T}\mathbf{y})} \|\mathbf{T}^{-1} \varepsilon(\mathbf{T}\mathbf{y})\|^2 = (\mathbb{E}_\eta \eta^2) \|\mathbf{T}^{-1}\|_{\text{F}}^2 \mathbb{E}_{\mathbf{y}} \|\mathbf{T}\mathbf{y}\|_\infty^2 \quad (24)$$

with detailed steps in Eq. (45).

We can obtain a lower bound for the term $\|\mathbf{T}^{-1}\|_{\text{F}}^2$ in Eq. (24).

$$\|\mathbf{T}^{-1}\|_{\text{F}}^2 \geq \text{tr} (\mathbf{S}^2 \mathbf{S}'^{-2}), \quad (25)$$

and the equality is attained when $\mathbf{R} = \mathbf{I}$, with detailed steps in Eqs. (46), (47).

Next, we obtain near-optimal lower and upper bounds for the term $\mathbb{E}_{\mathbf{y}} \|\mathbf{T}\mathbf{y}\|_\infty^2$ in Eq. (24) by choosing $\mathbf{U}' = \mathbf{H}$.

$$d^{-1} \text{tr} (\mathbf{S}'^2) \leq \mathbb{E}_{\mathbf{y}} \|\mathbf{T}\mathbf{y}\|_\infty^2 \leq \begin{cases} d^{o(1)-1} \text{tr} (\mathbf{S}'^2), & \text{tail-bounded } \mathcal{D}_{\mathbf{y}}, \\ \text{tr} (\mathbf{S}'^2), & \text{otherwise.} \end{cases} \quad (26)$$

Note that the upper bound is tighter when $\mathcal{D}_{\mathbf{y}}$ is a tail-bounded (zero-mean multivariate Gaussian or Laplacian) distribution than for a general distribution. For the full derivations of these bounds, please refer to Eqs. (48) to (57).

Taken Eqs. (25), (26) together, by setting $\mathbf{R} = \mathbf{I}$ and $\mathbf{U}' = \mathbf{H}$, the term $\|\mathbf{T}^{-1}\|_{\text{F}}^2 \mathbb{E}_{\mathbf{y}} \|\mathbf{T}\mathbf{y}\|_\infty^2$ is bounded by $\text{tr} (\mathbf{S}^2 \mathbf{S}'^{-2}) \text{tr} (\mathbf{S}'^2)$ within a gap of d such that

$$d^{-1} \text{tr} (\mathbf{S}^2 \mathbf{S}'^{-2}) \text{tr} (\mathbf{S}'^2) \leq \|\mathbf{T}^{-1}\|_{\text{F}}^2 \mathbb{E}_{\mathbf{y}} \|\mathbf{T}\mathbf{y}\|_\infty^2 \leq \text{tr} (\mathbf{S}^2 \mathbf{S}'^{-2}) \text{tr} (\mathbf{S}'^2). \quad (27)$$

And for a tail-bounded \mathcal{D}_y , the gap is narrowed to $d^{o(1)}$ such that

$$\|\mathbf{T}^{-1}\|_{\text{F}}^2 \mathbb{E}_y \|\mathbf{T}\mathbf{y}\|_{\infty}^2 = d^{o(1)-1} \text{tr}(\mathbf{S}^2 \mathbf{S}'^{-2}) \text{tr}(\mathbf{S}'^2). \quad (28)$$

By the Cauchy-Schwarz inequality, the lower bound of the trace product term is

$$\text{tr}(\mathbf{S}^2 \mathbf{S}'^{-2}) \text{tr}(\mathbf{S}'^2) \geq \left(\text{tr} \left((\mathbf{S}^2 \mathbf{S}'^{-2})^{\frac{1}{2}} (\mathbf{S}'^2)^{\frac{1}{2}} \right) \right)^2 = (\text{tr}(\mathbf{S}))^2. \quad (29)$$

and the equality is attained when $\mathbf{S}' \propto \mathbf{S}^{\frac{1}{2}}$. Without loss of generality, we can choose $\mathbf{S}' = \mathbf{S}^{\frac{1}{2}}$ to minimize both the lower and upper bounds in Eqs. (27), (28), and the quantization loss in Eq. (24) becomes near-optimal:

$$d^{-1} (\text{tr}(\mathbf{S}))^2 \leq \|\mathbf{T}^{-1}\|_{\text{F}}^2 \mathbb{E}_y \|\mathbf{T}\mathbf{y}\|_{\infty}^2 \leq \begin{cases} d^{o(1)-1} (\text{tr}(\mathbf{S}))^2, & \text{tail-bounded } \mathcal{D}_y, \\ (\text{tr}(\mathbf{S}))^2, & \text{otherwise.} \end{cases} \quad (30)$$

4.3.3 DISCUSSION

Consider the case of \mathbf{T} being orthogonal. For any general distribution \mathcal{D}_y , the bounds are

$$\text{tr}(\mathbf{S}^2) \leq \|\mathbf{T}^{-1}\|_{\text{F}}^2 \mathbb{E}_y \|\mathbf{T}\mathbf{y}\|_{\infty}^2 \leq d \text{tr}(\mathbf{S}^2) \quad (31)$$

with detailed steps in Eq. (58). For a tail-bounded \mathcal{D}_y , the Hadamard $\mathbf{T} = \mathbf{H}$ is empirically the best orthogonal transform, so the bounds can be tightened to

$$\|\mathbf{T}^{-1}\|_{\text{F}}^2 \mathbb{E}_y \|\mathbf{T}\mathbf{y}\|_{\infty}^2 = d^{o(1)} \text{tr}(\mathbf{S}^2) \quad (32)$$

Comparing Eq. (30) with Eqs. (31), (32) using the inequality Eq. (17), an orthogonal \mathbf{T} is suboptimal, and the error bounds of the Hadamard $\mathbf{T} = \mathbf{H}$ can be at most d times larger than those of the optimal \mathbf{T} , in the extreme outlier scenario. Figure 1 (right two columns) provides visualizations of different transforms.

5 GPU Kernel Support

As noted in Eq. (10), part of the WUSH transform has to be applied online during inference, requiring a specialized GPU kernel. Online blockwise *Hadamard* rotations are efficiently supported in MR-GPTQ’s kernels (Egiazarian et al., 2025). Yet, in their case, the transforms are data-independent, so it is possible to reuse a single transform across all blocks. By contrast, WUSH assigns a *distinct* transform to each block. This per-block specialization significantly complicates kernel reuse and fusion in existing low-level libraries.

Implementation. A first design decision is the storage layout of the WUSH matrices. For block size \mathbf{G} and number of blocks \mathbf{C} , we store matrices as $(\mathbf{G}, \mathbf{G}, \mathbf{C})$, i.e., transposed with respect to the channel dimension. Since this transposition is performed offline, it does not introduce any runtime overhead. This layout choice is motivated by the observation that, for small group sizes (e.g., $\mathbf{G}=32$ for MXFP4), the WUSH transformation is memory-bound. Accordingly, the proposed kernel formulates the operation as a GEMM-equivalent

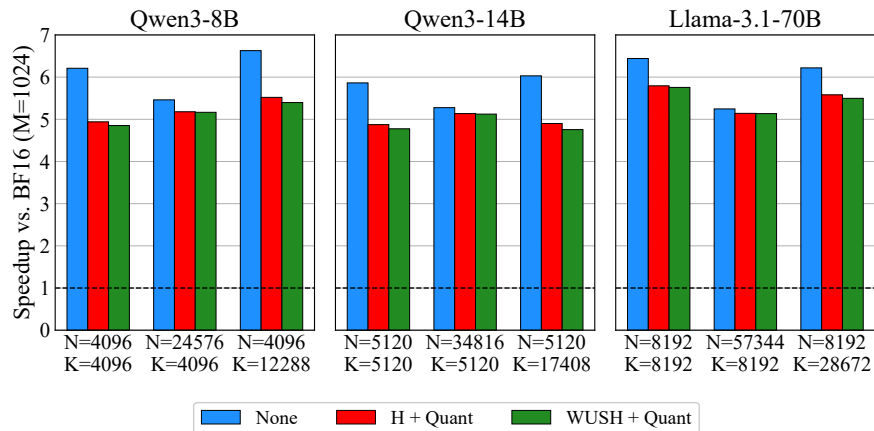


Figure 2: **Per-layer MXFP4 (group size $G=32$) GEMM speedups relative to BF16 at batch size $M=1024$ for Qwen3-8B, Qwen3-14B, and Llama-3.1-70B.** We compare kernels without transform or quantization (None), with Hadamard and quantization (H + Quant), and with WUSH and quantization (WUSH + Quant). For block size G and a layer with $K=C \times G$ input and N output channels, the Hadamard matrix size is (G, G) , while the WUSH size is (G, G, C) . For H + Quant, the QuTLASS implementation is used (Egiazarian et al., 2025), which also fuses the transform with the quantization step.

computation, corresponding to C independent dense Hadamard-like transforms. Each thread block processes a $\text{Tile}_M \times G$ subproblem, where Tile_M denotes the tile size along the batch dimension. Crucially, each block only needs to load a single (G, G) matrix to produce its output, matching the H + Quant case, maximizing effective bandwidth utilization.

The kernel is implemented using a CUTLASS GEMM template. The outer dimension M of the activation tensor (with shape (M, K)) and the outer dimension G of the WUSH matrix (with shape (G, G, C)) are mapped to the M and N dimensions of the GEMM, respectively. The internal GEMM dimension K' is fixed to G , rather than $G \times C$. The index C is instead handled implicitly as an offset that each thread block applies based on the specific K/G subproblem it is assigned to.

Performance. Figure 2 reports per-layer GEMM speedups on RTX 5090 at batch size 1024 for Qwen3-8B, Qwen3-14B, and Llama-3.1-70B, normalized to BF16. Across all models and layer shapes, MXFP4 kernels achieve speedups of up to $6.63 \times$ over BF16, compared to the theoretical peak of $8 \times$ on this GPU. When including the transform and quantization overhead, the WUSH + Quant kernels closely match the performance of the optimized H + Quant baseline, with an average throughput difference of only 1.3%. Remarkably, in some configurations, WUSH + Quant achieves identical performance to H + Quant. This negligible difference arises from loading C transform matrices instead of a single one; however, it is almost entirely mitigated by the kernel design and effective reuse via the L1 and L2 caches. The remaining gap to the no-quantization upper bound indicates that performance is primarily limited by quantization overhead associated with reading and

writing the activation matrix, rather than the choice of transform. These results demonstrate that WUSH introduces negligible additional costs.

6 Experiments

Setup. We now present experiments evaluating the layer-wise losses and the accuracy of quantized models using the WUSH transform, relative to SmoothQuant (Xiao et al., 2023), QuaRot (Ashkboos et al., 2024b), SpinQuant (Liu et al., 2025), and MR-GPTQ (Egiazarian et al., 2025) baselines. MR-GPTQ is the current state-of-the-art for MXFP/NVFP quantization. We conduct experiments on the LLama-3.2-3B-Instruct, LLama-3.1-8B-Instruct, and Qwen3-8B/14B/32B models. We use Platinum Benchmarks (Vendrow et al., 2025) and the LM Evaluation Harness (Gao et al., 2021) for accuracy evaluation.

6.1 Superior Per-Layer Layer Loss

Table 1: Layerwise RTN quantization loss in the scale of 10^{-3} .

		Q	K	V	O	G	U	D
MXFP4	I	11.1	12.0	10.7	4.35	7.10	6.56	5.47
	R	7.61	7.73	9.14	3.84	5.56	5.68	4.07
	H	7.24	7.20	8.60	3.79	5.45	5.61	3.90
	WUS	6.27	7.22	4.05	3.57	5.76	4.75	4.46
	WUSH	3.34	3.34	3.30	2.76	4.49	4.39	3.39
NVFP4	I	4.23	4.35	4.37	2.34	3.49	3.41	2.41
	R	4.98	5.01	5.86	2.54	3.63	3.68	2.66
	H	5.60	5.62	6.70	2.58	3.71	3.79	2.78
	WUS	2.26	2.36	2.30	2.00	3.04	3.01	2.23
	WUSH	2.40	2.44	2.28	1.92	3.09	3.02	2.33
INT4	I	170.	123.	13.2	4.55	55.9	9.83	19.3
	R	5.79	5.84	6.96	2.94	4.22	4.29	3.10
	H	5.57	5.55	6.80	2.86	4.09	4.25	3.03
	WUS	213.	142.	10.7	4.54	50.2	7.42	13.1
	WUSH	2.39	2.43	2.54	2.10	3.43	3.43	2.55

We first report the layerwise weight-activation RTN quantization loss (L_2 loss normalized by the number of elements) for each linear layer (attention projection layers Q, K, V, O and MLP projection layers Gate (G), Up (U), Down (D)) in the 18th transformer block of Qwen3-8B, using 32 calibration samples of sequence length 2048 from the FineWeb-Edu dataset (Penedo et al., 2024). We found the results to be consistent across blocks and datasets. We compare the WUSH transform with the identity (I), random rotation (R) averaged over 10 runs, Hadamard (H), and WUSH without Hadamard (WUS). Table 1 summarizes the losses for MXFP4, NVFP4, and INT4 formats, where INT4 denotes 4-bit integers with Gaussian MSE clipping and BF16 scales of group size 32. Across formats, WUSH substantially reduces the

loss: WUSH consistently yields the smallest loss for MXFP4 and INT4, while WUSH and WUS are almost equally optimal for NVFP4. The errors for NVFP4 tend to be lower due to its group size of 16.

These trends confirm our theory, suggesting that the assumptions (Section 4.1) and modeling (Sections 4.2.1 and 4.3.1) capture the dominant sources of error. At the same time, MXFP4 behaves as a hybrid between ideal FP and INT quantization: the effective mantissa step changes uniformly, imparting INT-like behavior, especially in the subnormal regime and small exponent ranges. This explains why Hadamard transforms provide measurable gains for MXFP4, despite the ideal FP theory (Section 4.2.3) predicting no benefit for purely orthogonal transforms. For NVFP4, the Hadamard alone is harmful due to the top-element preservation effect of this format (Egiazarian et al., 2025). Remarkably, other components in WUSH overcome this effect and produce smaller losses than the identity transform.

6.2 End-to-end LLM Accuracy Benchmarks

Table 2: Llama-3.1-8B-Instruct W4A4 accuracy results on the LM Evaluation Harness under different methods.

Format	Method	MMLU-CoT	GSM8K	HellaSwag	WinoGrande	Average	Recovery
BF16	-	72.76	85.06	80.01	77.90	78.93	100.0
NVFP4	RTN-I	68.26	78.39	78.15	74.11	74.73	94.67
	RTN-H	67.41	78.01	77.31	73.48	74.05	93.82
	SmoothQuant	68.90	79.50	79.50	74.70	75.70	95.90
	QuaRot	66.50	77.40	77.25	75.14	74.10	93.80
	SpinQuant	66.50	76.10	76.96	75.32	73.70	93.40
	GPTQ-I	68.85	82.60	78.26	74.51	75.72	95.92
	GPTQ-H (MR-GPTQ)	69.12	80.80	78.17	75.24	75.84	96.08
	RTN-WUSH	68.83	78.57	78.22	75.47	75.28	95.37
	GPTQ-WUSH	69.69	80.11	78.52	76.09	76.10	96.40
MXFP4	RTN-I	62.21	67.85	73.99	73.24	69.32	87.83
	RTN-H	62.38	72.48	75.29	71.67	70.45	89.26
	SmoothQuant	63.93	68.54	75.10	73.56	70.30	89.06
	QuaRot	49.86	56.94	73.50	71.43	62.90	79.70
	SpinQuant	61.80	68.16	74.87	72.93	69.40	88.00
	GPTQ-I	63.49	68.46	76.01	74.51	70.62	89.47
	GPTQ-H (MR-GPTQ)	67.19	75.70	76.91	74.80	73.65	93.31
	RTN-WUSH	66.85	75.16	77.28	73.56	73.21	92.75
	GPTQ-WUSH	67.79	77.41	77.44	74.78	74.35	94.20

Table 2 compares WUSH relative to prior works for Llama-3.1-8B-Instruct on LM Evaluation Harness metrics, in the same setup as Egiazarian et al. (2025). Overall, WUSH consistently yields the best results, by a large margin for MXFP4. On Qwen3-8B measured on Platinum Benchmarks (Figure 3), WUSH improves MXFP4 by up to +1.3 (RTN) and +0.7 (GPTQ) average points, while NVFP4 improvements are smaller and often within run-to-run variability. Results (Tables 3 and 4 and Figures 6 to 9) for additional models are in Appendix Section B.

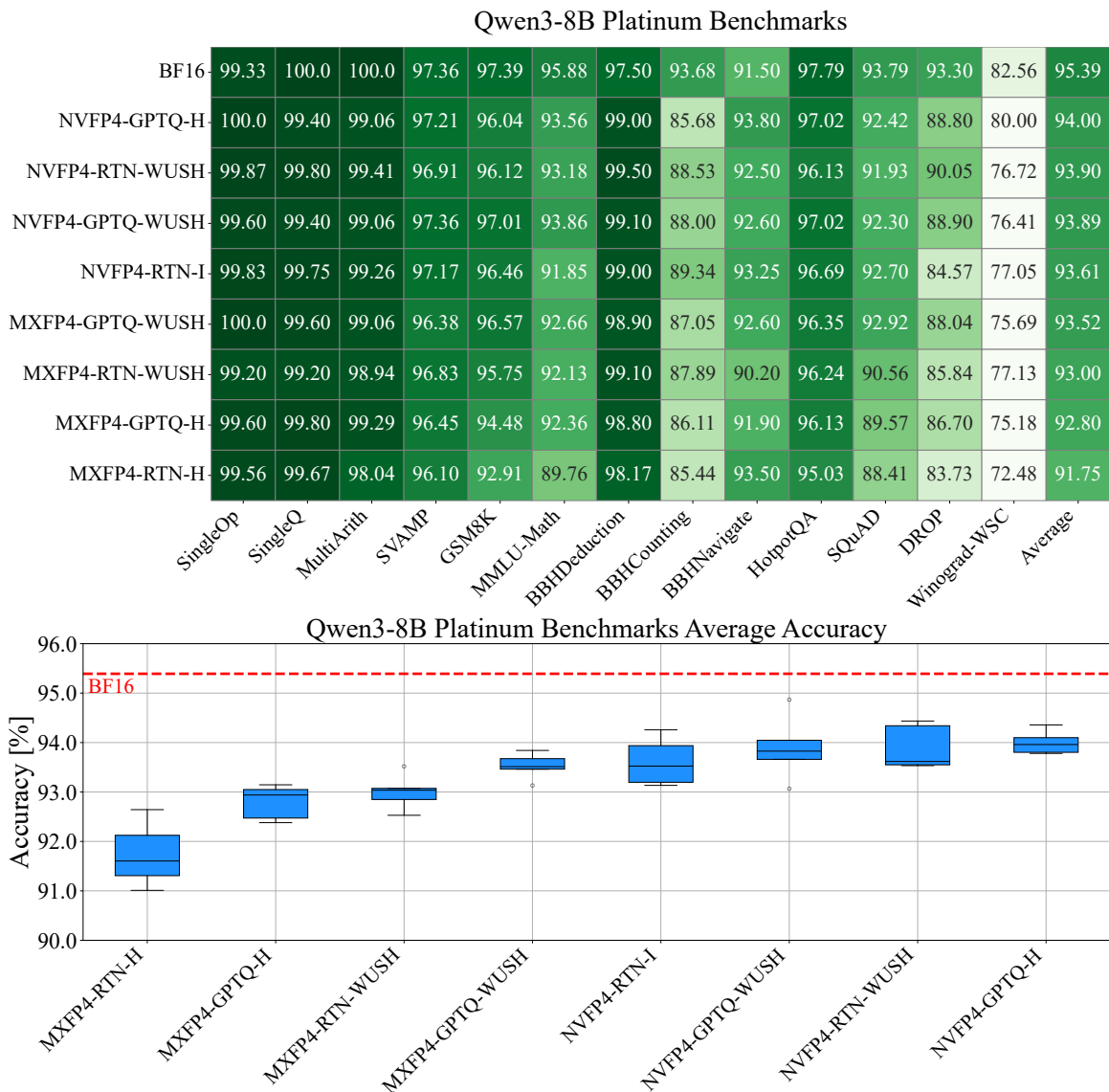


Figure 3: Comparison of different transforms on Qwen3-8B.

Table 4 shows the LM Evaluation Harness results for different models, e.g., for Qwen3-14B WUSH reduces the NVFP4-MXFP4 average gap to 0.36 points, and above 98% recovery. Figures 6 to 9 also reflect similar trends. We conclude that WUSH improves the state-of-the-art for weight-activation quantization.

7 Future Work

It will be useful to explore structurally simplified variants of WUSH that trade optimality for a reduction in the cost of applying the transforms at inference time. One promising avenue is to approximate the data-aware component with a diagonal matrix.

8 Conclusion

We have studied weight-activation quantization for LLMs in the presence of heavy-tailed outliers and have shown that this problem admits closed-form linear transforms for both FP and INT block quantizers. Our construction, WUSH, combines a fixed Hadamard backbone with a data-aware component derived from second-order statistics, yielding a non-orthogonal blockwise transform that is provably near-optimal and remains amenable to efficient GPU kernel implementations. These results clarify the empirical success of Hadamard rotations and indicate that principled, data-aware block transforms can yield significant improvements, e.g., making the MXFP format competitive with NVFP.

Acknowledgment

We would like to thank Tijmen Blankevoort for useful discussions and for suggesting the name WUSH, which is a clear improvement over our previous name (HSUW).

References

- Saleh Ashkboos, Iliia Markov, Elias Frantar, Tingxuan Zhong, Xincheng Wang, Jie Ren, Torsten Hoefler, and Dan Alistarh. QUIK: Towards end-to-end 4-bit inference on generative large language models. In Yaser Al-Onaizan, Mohit Bansal, and Yun-Nung Chen (eds.), *Proceedings of the 2024 Conference on Empirical Methods in Natural Language Processing*, pp. 3355–3371, Miami, Florida, USA, November 2024a. Association for Computational Linguistics. doi: 10.18653/v1/2024.emnlp-main.197. URL <https://aclanthology.org/2024.emnlp-main.197/>. 2
- Saleh Ashkboos, Amirkeivan Mohtashami, Maximilian L. Croci, Bo Li, Pashmina Cameron, Martin Jaggi, Dan Alistarh, Torsten Hoefler, and James Hensman. Quarot: Outlier-free 4-bit inference in rotated llms. In A. Globerson, L. Mackey, D. Belgrave, A. Fan, U. Paquet, J. Tomczak, and C. Zhang (eds.), *Advances in Neural Information Processing Systems*, volume 37, pp. 100213–100240. Curran Associates, Inc., 2024b. doi: 10.52202/079017-3180. URL https://proceedings.neurips.cc/paper_files/paper/2024/file/b5b939436789f76f08b9d0da5e81af7c-Paper-Conference.pdf. 1, 3, 13
- Jerry Chee, Yaohui Cai, Volodymyr Kuleshov, and Christopher M De Sa. Quip: 2-bit quantization of large language models with guarantees. In A. Oh, T. Naumann, A. Globerson, K. Saenko, M. Hardt, and S. Levine (eds.), *Advances in Neural Information Processing Systems*, volume 36, pp. 4396–4429. Curran Associates, Inc., 2023. URL https://proceedings.neurips.cc/paper_files/paper/2023/file/0df38cd13520747e1e64e5b123a78ef8-Paper-Conference.pdf. 1, 3
- Jiale Chen, Yalda Shabanzadeh, Elvir Crnčević, Torsten Hoefler, and Dan Alistarh. The geometry of llm quantization: Gptq as babai’s nearest plane algorithm, 2025. URL <https://arxiv.org/abs/2507.18553>. 2, 6

- Alexandre Défossez, Yossi Adi, and Gabriel Synnaeve. Differentiable model compression via pseudo quantization noise. *Transactions on Machine Learning Research*, 2022. ISSN 2835-8856. URL <https://openreview.net/forum?id=DijnKziche>. 28
- Tim Dettmers, Mike Lewis, Younes Belkada, and Luke Zettlemoyer. Gpt3.int8(): 8-bit matrix multiplication for transformers at scale. In S. Koyejo, S. Mohamed, A. Agarwal, D. Belgrave, K. Cho, and A. Oh (eds.), *Advances in Neural Information Processing Systems*, volume 35, pp. 30318–30332. Curran Associates, Inc., 2022. URL https://proceedings.neurips.cc/paper_files/paper/2022/file/c3ba4962c05c49636d4c6206a97e9c8a-Paper-Conference.pdf. 1, 2
- Tim Dettmers, Ruslan A. Svirschevski, Vage Egiazarian, Denis Kuznedelev, Elias Frantar, Saleh Ashkboos, Alexander Borzunov, Torsten Hoefler, and Dan Alistarh. SpQR: A sparse-quantized representation for near-lossless LLM weight compression. In *The Twelfth International Conference on Learning Representations*, 2024. URL <https://openreview.net/forum?id=Q1u25ahSuy>. 2
- Vage Egiazarian, Roberto L. Castro, Denis Kuznedelev, Andrei Panferov, Eldar Kurtic, Shubhra Pandit, Alexandre Marques, Mark Kurtz, Saleh Ashkboos, Torsten Hoefler, and Dan Alistarh. Bridging the gap between promise and performance for microscaling fp4 quantization, 2025. URL <https://arxiv.org/abs/2509.23202>. 1, 3, 11, 12, 13, 14
- Elias Frantar and Dan Alistarh. Optimal brain compression: A framework for accurate post-training quantization and pruning. In S. Koyejo, S. Mohamed, A. Agarwal, D. Belgrave, K. Cho, and A. Oh (eds.), *Advances in Neural Information Processing Systems*, volume 35, pp. 4475–4488. Curran Associates, Inc., 2022. URL https://proceedings.neurips.cc/paper_files/paper/2022/file/1caf09c9f4e6b0150b06a07e77f2710c-Paper-Conference.pdf. 2
- Elias Frantar, Saleh Ashkboos, Torsten Hoefler, and Dan Alistarh. OPTQ: Accurate quantization for generative pre-trained transformers. In *The Eleventh International Conference on Learning Representations*, 2023. URL <https://openreview.net/forum?id=tcbBPnfwxS>. 1, 2, 6
- Leo Gao, Jonathan Tow, Stella Biderman, Sid Black, Anthony DiPofi, Charles Foster, Laurence Golding, Jeffrey Hsu, Kyle McDonell, Niklas Muennighoff, Jason Phang, Laria Reynolds, Eric Tang, Anish Thite, Ben Wang, Kevin Wang, and Andy Zou. A framework for few-shot language model evaluation, September 2021. URL <https://doi.org/10.5281/zenodo.5371629>. 13
- Herve Jegou, Matthijs Douze, and Cordelia Schmid. Hamming embedding and weak geometric consistency for large scale image search. In David Forsyth, Philip Torr, and Andrew Zisserman (eds.), *Computer Vision – ECCV 2008*, pp. 304–317, Berlin, Heidelberg, 2008. Springer Berlin Heidelberg. ISBN 978-3-540-88682-2. URL https://link.springer.com/chapter/10.1007/978-3-540-88682-2_24. 1
- Herve Jégou, Matthijs Douze, and Cordelia Schmid. Product quantization for nearest neighbor search. *IEEE Transactions on Pattern Analysis and Machine Intelligence*, 33(1):

- 117–128, 2011. doi: 10.1109/TPAMI.2010.57. URL <https://ieeexplore.ieee.org/document/5432202>. 1
- Eldar Kurtic, Alexandre Noll Marques, Shubhra Pandit, Mark Kurtz, and Dan Alistarh. “give me BF16 or give me death”? accuracy-performance trade-offs in LLM quantization. In Wanxiang Che, Joyce Nabende, Ekaterina Shutova, and Mohammad Taher Pilehvar (eds.), *Proceedings of the 63rd Annual Meeting of the Association for Computational Linguistics (Volume 1: Long Papers)*, pp. 26872–26886, Vienna, Austria, July 2025. Association for Computational Linguistics. ISBN 979-8-89176-251-0. doi: 10.18653/v1/2025.acl-long.1304. URL <https://aclanthology.org/2025.acl-long.1304/>. 1
- Ji Lin, Jiaming Tang, Haotian Tang, Shang Yang, Wei-Ming Chen, Wei-Chen Wang, Guangxuan Xiao, Xingyu Dang, Chuang Gan, and Song Han. Awq: Activation-aware weight quantization for on-device llm compression and acceleration. In P. Gibbons, G. Pekhimenko, and C. De Sa (eds.), *Proceedings of Machine Learning and Systems*, volume 6, pp. 87–100, 2024. URL https://proceedings.mlsys.org/paper_files/paper/2024/file/42a452cbafa9dd64e9ba4aa95cc1ef21-Paper-Conference.pdf. 1, 3
- Zechun Liu, Changsheng Zhao, Igor Fedorov, Bilge Soran, Dhruv Choudhary, Raghuraman Krishnamoorthi, Vikas Chandra, Yuandong Tian, and Tijmen Blankevoort. Spinqant: LLM quantization with learned rotations. In *The Thirteenth International Conference on Learning Representations*, 2025. URL <https://openreview.net/forum?id=og06DGE6FZ>. 1, 2, 3, 13
- Open Compute Project Foundation MX Alliance. OCP Microscaling Formats (MX) Specification Version 1.0. Technical specification, Open Compute Project Foundation, September 2023. URL <https://www.opencompute.org/documents/ocp-microscaling-formats-mx-v1-0-spec-final-pdf>. 3
- NVIDIA. Nvidia blackwell architecture technical brief. Technical report, NVIDIA, 2024. URL <https://resources.nvidia.com/en-us-blackwell-architecture>. 3
- Guilherme Penedo, Hynek Kydlíček, Loubna Ben allal, Anton Lozhkov, Margaret Mitchell, Colin Raffel, Leandro Von Werra, and Thomas Wolf. The fineweb datasets: Decanting the web for the finest text data at scale. In A. Globerson, L. Mackey, D. Belgrave, A. Fan, U. Paquet, J. Tomczak, and C. Zhang (eds.), *Advances in Neural Information Processing Systems*, volume 37, pp. 30811–30849. Curran Associates, Inc., 2024. doi: 10.52202/079017-0970. URL https://proceedings.neurips.cc/paper_files/paper/2024/file/370df50ccfd8bde18f8f9c2d9151bda-Paper-Datasets_and_Benchmarks_Track.pdf. 13
- Yuantian Shao, Peisong Wang, Yuanteng Chen, Chang Xu, Zhihui Wei, and Jian Cheng. Block rotation is all you need for mxfp4 quantization, 2025. URL <https://arxiv.org/abs/2511.04214>. 3
- Yuxuan Sun, Ruikang Liu, Haoli Bai, Han Bao, Kang Zhao, Yuening Li, Jiaxin Hu, Xianzhi Yu, Lu Hou, Chun Yuan, Xin Jiang, Wulong Liu, and Jun Yao. FlatQuant: Flatness matters for LLM quantization. In Aarti Singh, Maryam Fazel, Daniel Hsu, Simon Lacoste-Julien, Felix Berkenkamp, Tegan Maharaj, Kiri Wagstaff, and Jerry Zhu (eds.), *Proceedings*

- of the 42nd International Conference on Machine Learning, volume 267 of *Proceedings of Machine Learning Research*, pp. 57587–57613. PMLR, 13–19 Jul 2025. URL <https://proceedings.mlr.press/v267/sun251.html>. 2, 3
- Albert Tseng, Jerry Chee, Qingyao Sun, Volodymyr Kuleshov, and Christopher De Sa. QuIP#: Even better LLM quantization with hadamard incoherence and lattice codebooks. In Ruslan Salakhutdinov, Zico Kolter, Katherine Heller, Adrian Weller, Nuria Oliver, Jonathan Scarlett, and Felix Berkenkamp (eds.), *Proceedings of the 41st International Conference on Machine Learning*, volume 235 of *Proceedings of Machine Learning Research*, pp. 48630–48656. PMLR, 21–27 Jul 2024a. URL <https://proceedings.mlr.press/v235/tseng24a.html>. 1, 3
- Albert Tseng, Qingyao Sun, David Hou, and Christopher De. Qtip: Quantization with trellises and incoherence processing. In A. Globerson, L. Mackey, D. Belgrave, A. Fan, U. Paquet, J. Tomczak, and C. Zhang (eds.), *Advances in Neural Information Processing Systems*, volume 37, pp. 59597–59620. Curran Associates, Inc., 2024b. doi: 10.52202/079017-1904. URL https://proceedings.neurips.cc/paper_files/paper/2024/file/6de2e84b8da47bb2eb5e2ac96c63d2b0-Paper-Conference.pdf. 3
- Joshua Vendrow, Edward Vendrow, Sara Beery, and Aleksander Madry. Do large language model benchmarks test reliability?, 2025. URL <https://arxiv.org/abs/2502.03461>. 13
- Guangxuan Xiao, Ji Lin, Mickael Seznec, Hao Wu, Julien Demouth, and Song Han. SmoothQuant: Accurate and efficient post-training quantization for large language models. In Andreas Krause, Emma Brunskill, Kyunghyun Cho, Barbara Engelhardt, Sivan Sabato, and Jonathan Scarlett (eds.), *Proceedings of the 40th International Conference on Machine Learning*, volume 202 of *Proceedings of Machine Learning Research*, pp. 38087–38099. PMLR, 23–29 Jul 2023. URL <https://proceedings.mlr.press/v202/xiao23c.html>. 1, 3, 13

Appendix A. Detailed Theoretical Results

A.1 Second Moment Decompositions

Lemma 2 (Invariance of the Decomposition Choices) *For any full rank $\mathbf{W}'_{(i)}, \mathbf{X}'_{(i)}$ that satisfy Eq. (6), the matrix products $\mathbf{W}'_{(i)}\mathbf{U}_{(i)}$ and $\mathbf{X}'_{(i)}\mathbf{V}_{(i)}$ in Eq. (8) are invariant up to sign and permutation changes.*

Proof We omit the subscript (i) and superscript $'$ to simplify notation.

Let $\hat{\mathbf{W}}, \hat{\mathbf{X}} \in \mathbb{R}^{d \times d}$ such that $\hat{\mathbf{W}}\hat{\mathbf{W}}^\top = \mathbf{W}\mathbf{W}^\top$ and $\hat{\mathbf{X}}\hat{\mathbf{X}}^\top = \mathbf{X}\mathbf{X}^\top$. Define $\mathbf{Q}_W = \mathbf{W}^{-1}\hat{\mathbf{W}}$ and $\mathbf{Q}_X = \mathbf{X}^{-1}\hat{\mathbf{X}}$. Then,

$$\mathbf{Q}_W\mathbf{Q}_W^\top = \mathbf{W}^{-1}\hat{\mathbf{W}}\hat{\mathbf{W}}^\top\mathbf{W}^{-\top} = \mathbf{W}^{-1}(\mathbf{W}\mathbf{W}^\top)\mathbf{W}^{-\top} = \mathbf{I}, \quad (33)$$

and similarly $\mathbf{Q}_X\mathbf{Q}_X^\top = \mathbf{I}$. Hence $\mathbf{Q}_W, \mathbf{Q}_X$ are orthogonal and $\hat{\mathbf{W}} = \mathbf{W}\mathbf{Q}_W, \hat{\mathbf{X}} = \mathbf{X}\mathbf{Q}_X$. By Eq. (7), we have $\mathbf{U}, \mathbf{S}, \mathbf{V} \in \mathbb{R}^{d \times d}$ as the SVD of $\mathbf{W}^\top\mathbf{X} = \mathbf{U}\mathbf{S}\mathbf{V}^\top$. Therefore,

$$\hat{\mathbf{W}}^\top\hat{\mathbf{X}} = \mathbf{Q}_W^\top\mathbf{W}^\top\mathbf{X}\mathbf{Q}_X = \mathbf{Q}_W^\top(\mathbf{U}\mathbf{S}\mathbf{V}^\top)\mathbf{Q}_X = (\mathbf{Q}_W^\top\mathbf{U})\mathbf{S}(\mathbf{Q}_X^\top\mathbf{V})^\top. \quad (34)$$

Thus, we may take $\hat{\mathbf{U}} = \mathbf{Q}_W^\top\mathbf{U}, \hat{\mathbf{S}} = \mathbf{S}, \hat{\mathbf{V}} = \mathbf{Q}_X^\top\mathbf{V}$ (up to the sign and permutation conventions) as the SVD of $\hat{\mathbf{W}}^\top\hat{\mathbf{X}} = \hat{\mathbf{U}}\hat{\mathbf{S}}\hat{\mathbf{V}}^\top$. With this,

$$\begin{aligned} \hat{\mathbf{W}}\hat{\mathbf{U}} &= \mathbf{W}\mathbf{Q}_W\mathbf{Q}_W^\top\mathbf{U} = \mathbf{W}\mathbf{U}, \\ \hat{\mathbf{X}}\hat{\mathbf{V}} &= \mathbf{X}\mathbf{Q}_X\mathbf{Q}_X^\top\mathbf{V} = \mathbf{X}\mathbf{V}. \end{aligned} \quad (35)$$

■

A.2 Multivariate vs. Univariate Probabilistic Modeling

A common intuition in prior transform-based quantization methods is largely univariate: apply an orthogonal mixing (Hadamard or learned rotation) so that the distribution of coordinate-wise values becomes more ‘‘Gaussian-like,’’ thereby reducing the impact of heavy-tailed outliers. In contrast, our probabilistic modeling is explicitly multivariate: we model a quantization group as a joint random vector and reason about its second-order structure, enabling analysis in the eigenbasis and construction of transforms that depend on the spectrum (eigenvalues / singular values).

Figure 4 illustrates the key limitation of purely orthogonal ‘‘Gaussianization.’’ In the top row (original distributions), the joint density is anisotropic: the two coordinate-wise marginals differ in spread, and their average can appear heavy-tailed or non-Gaussian depending on the axis alignment. In the bottom row, after the Hadamard (45° rotation) transform, the coordinate marginals become nearly identical, and the average marginal appears more Gaussian-like. However, this does not imply that outliers have been removed in the underlying multivariate geometry: orthogonal transforms preserve global energy and, crucially, preserve

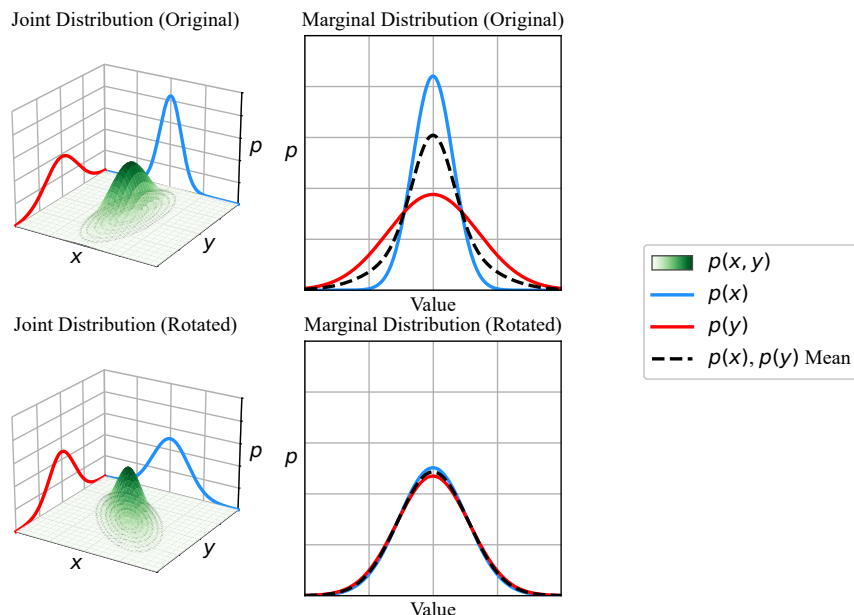


Figure 4: **Rotation can equalize marginals without alleviating multivariate outliers.** Top: an anisotropic 2D distribution with unequal coordinate marginals. Bottom: after an orthogonal rotation, the two marginals become nearly identical, and their average appears more Gaussian-like. Nevertheless, the joint distribution retains the same eigenvalues (spectrum) under rotation, so extreme points remain extreme in the multivariate space; they are merely “hidden” from any single marginal view. This motivates multivariate, spectrum-aware transforms that act on the joint geometry rather than relying on marginal “Gaussianization.”

the eigenvalues of the covariance (they only rotate eigenvectors). Consequently, points that are extreme in the principal directions remain extreme in the joint space, even if they are less visually apparent in any single marginal.

This distinction is central to group quantization. Quantization error is driven by joint properties (e.g., how mass concentrates along dominant directions and how extreme points interact with group-wise scaling), which cannot be certified by marginal statistics alone. Our multivariate formulation therefore targets the spectrum directly: by exposing and using the eigen-/singular-value structure of the group statistics, we can design transforms that genuinely reduce the effective anisotropy responsible for outlier-dominated scaling, rather than merely redistributing it across coordinates via rotations.

A.3 Equation Derivations

Standard basis vector notation.

Denote the k -th standard basis vector as $\mathbf{e}_k \in \{0, 1\}^d$, where the k -th element is 1 and 0 otherwise.

Basic second-order expectations.

$$\begin{aligned}
\mathbb{E}_y \mathbf{y} \mathbf{y}^\top &= \mathbf{W}'^\top \left(\mathbb{E}_x \mathbf{x} \mathbf{x}^\top \right) \mathbf{W}' = \mathbf{W}'^\top \mathbf{X}' \mathbf{X}'^\top \mathbf{W}' && \text{(Eq. (12))} \\
&= \mathbf{U} \mathbf{S} \mathbf{V}^\top \mathbf{V} \mathbf{S} \mathbf{U}^\top = \mathbf{U} \mathbf{S}^2 \mathbf{U}^\top, && \text{(Eq. (7))} \\
\mathbb{E}_y \mathbf{T} \mathbf{y} (\mathbf{T} \mathbf{y})^\top &= \mathbf{T} \left(\mathbb{E}_y \mathbf{y} \mathbf{y}^\top \right) \mathbf{T}^\top \\
&= \mathbf{U}' \mathbf{S}' \mathbf{R}^\top \mathbf{S}^{-1} \mathbf{U}^\top \mathbf{U} \mathbf{S}^2 \mathbf{U}^\top \mathbf{U} \mathbf{S}^{-1} \mathbf{R} \mathbf{S}' \mathbf{U}'^\top = \mathbf{U}' \mathbf{S}'^2 \mathbf{U}'^\top, && \text{(Eq. (16))} \\
\mathbb{E}_y \|\mathbf{y}\|^2 &= \text{tr} \left(\mathbb{E}_y \mathbf{y} \mathbf{y}^\top \right) = \text{tr} \left(\mathbf{U} \mathbf{S}^2 \mathbf{U}^\top \right) = \text{tr} \left(\mathbf{S}^2 \right), \\
\mathbb{E}_y \|\mathbf{T} \mathbf{y}\|^2 &= \text{tr} \left(\mathbf{T} \mathbf{y} (\mathbf{T} \mathbf{y})^\top \right) = \text{tr} \left(\mathbf{U}' \mathbf{S}'^2 \mathbf{U}'^\top \right) = \text{tr} \left(\mathbf{S}'^2 \right).
\end{aligned} \tag{36}$$

Eq. (13).

$$\begin{aligned}
\ell &= \mathbb{E}_{\mathbf{w}, \mathbf{x}, \varepsilon(\mathbf{T}_W \mathbf{w}), \varepsilon(\mathbf{T}_X \mathbf{x})} \left((\mathbf{T}_W \mathbf{w} + \varepsilon(\mathbf{T}_W \mathbf{w}))^\top (\mathbf{T}_X \mathbf{x} + \varepsilon(\mathbf{T}_X \mathbf{x})) - \mathbf{w}^\top \mathbf{x} \right)^2 \\
&= \mathbb{E}_{\mathbf{w}, \mathbf{x}, \varepsilon(\mathbf{T}_W \mathbf{w}), \varepsilon(\mathbf{T}_X \mathbf{x})} \left(\mathbf{x}^\top \mathbf{T}_X^\top \varepsilon(\mathbf{T}_W \mathbf{w}) + \mathbf{w}^\top \mathbf{T}_W^\top \varepsilon(\mathbf{T}_X \mathbf{x}) + \underbrace{\varepsilon(\mathbf{T}_W \mathbf{w})^\top \varepsilon(\mathbf{T}_X \mathbf{x})}_{\approx 0 \text{ (first order approx.)}} + \underbrace{\mathbf{w}^\top \mathbf{T}_W^\top \mathbf{T}_X \mathbf{x} - \mathbf{w}^\top \mathbf{x}}_{= 0 \text{ (}\mathbf{T}_W = \mathbf{T}_X^{-\top}\text{)}} \right)^2 \\
&\approx \mathbb{E}_{\mathbf{w}, \mathbf{x}, \varepsilon(\mathbf{T}_W \mathbf{w}), \varepsilon(\mathbf{T}_X \mathbf{x})} \left(\mathbf{x}^\top \mathbf{T}_X^\top \varepsilon(\mathbf{T}_W \mathbf{w}) + \mathbf{w}^\top \mathbf{T}_W^\top \varepsilon(\mathbf{T}_X \mathbf{x}) \right)^2 \\
&= \mathbb{E}_{\mathbf{w}, \mathbf{x}, \varepsilon(\mathbf{T}_W \mathbf{w}), \varepsilon(\mathbf{T}_X \mathbf{x})} \left(\mathbf{x}^\top \mathbf{T}_X^\top \varepsilon(\mathbf{T}_W \mathbf{w}) \right)^2 + \left(\mathbf{w}^\top \mathbf{T}_W^\top \varepsilon(\mathbf{T}_X \mathbf{x}) \right)^2 + \underbrace{\mathbf{x}^\top \mathbf{T}_X^\top \varepsilon(\mathbf{T}_W \mathbf{w})}_{\mathbb{E}(\cdot) = 0} \underbrace{\left(\mathbf{w}^\top \mathbf{T}_W^\top \varepsilon(\mathbf{T}_X \mathbf{x}) \right)}_{\mathbb{E}(\cdot) = 0} \\
&= \mathbb{E}_{\mathbf{w}, \mathbf{x}, \varepsilon(\mathbf{T}_W \mathbf{w}), \varepsilon(\mathbf{T}_X \mathbf{x})} \left(\mathbf{x}^\top \mathbf{T}_X^\top \varepsilon(\mathbf{T}_W \mathbf{w}) \right)^2 + \left(\mathbf{w}^\top \mathbf{T}_W^\top \varepsilon(\mathbf{T}_X \mathbf{x}) \right)^2 \\
&= \left(\mathbb{E}_{\mathbf{w}, \mathbf{x}, \varepsilon(\mathbf{T}_W \mathbf{w})} \varepsilon(\mathbf{T}_W \mathbf{w})^\top \mathbf{T}_X \underbrace{\mathbf{x} \mathbf{x}^\top \mathbf{T}_X^\top}_{\mathbb{E}_x \mathbf{x} \mathbf{x}^\top = \mathbf{X}' \mathbf{X}'^\top} \varepsilon(\mathbf{T}_W \mathbf{w}) \right) \\
&\quad + \left(\mathbb{E}_{\mathbf{w}, \mathbf{x}, \varepsilon(\mathbf{T}_X \mathbf{x})} \varepsilon(\mathbf{T}_X \mathbf{x})^\top \mathbf{T}_W \underbrace{\mathbf{w} \mathbf{w}^\top}_{\mathbb{E}_w \mathbf{w} \mathbf{w}^\top = \mathbf{W}' \mathbf{W}'^\top} \mathbf{T}_W^\top \varepsilon(\mathbf{T}_X \mathbf{x}) \right) \\
&= \left(\mathbb{E}_{\mathbf{w}, \varepsilon(\mathbf{T}_W \mathbf{w})} \varepsilon(\mathbf{T}_W \mathbf{w})^\top \mathbf{T}_X \mathbf{X}' \mathbf{X}'^\top \mathbf{T}_X^\top \varepsilon(\mathbf{T}_W \mathbf{w}) \right) \\
&\quad + \left(\mathbb{E}_{\mathbf{x}, \varepsilon(\mathbf{T}_X \mathbf{x})} \varepsilon(\mathbf{T}_X \mathbf{x})^\top \mathbf{T}_W \mathbf{W}' \mathbf{W}'^\top \mathbf{T}_W^\top \varepsilon(\mathbf{T}_X \mathbf{x}) \right) \\
&= \left(\mathbb{E}_{\mathbf{w}, \varepsilon(\mathbf{T}_W \mathbf{w})} \left\| \underbrace{\mathbf{X}'^\top \mathbf{T}_X^\top}_{= \mathbf{T}_W^{-1}} \varepsilon(\mathbf{T}_W \mathbf{w}) \right\|^2 \right) + \left(\mathbb{E}_{\mathbf{x}, \varepsilon(\mathbf{T}_X \mathbf{x})} \left\| \underbrace{\mathbf{W}'^\top \mathbf{T}_W^\top}_{= \mathbf{T}_X^{-1}} \varepsilon(\mathbf{T}_X \mathbf{x}) \right\|^2 \right) \\
&= \left(\mathbb{E}_{\mathbf{w}, \varepsilon(\mathbf{T}_W \mathbf{w})} \left\| \mathbf{X}'^\top \mathbf{T}_W^{-1} \varepsilon(\mathbf{T}_W \mathbf{w}) \right\|^2 \right) + \left(\mathbb{E}_{\mathbf{x}, \varepsilon(\mathbf{T}_X \mathbf{x})} \left\| \mathbf{W}'^\top \mathbf{T}_X^{-1} \varepsilon(\mathbf{T}_X \mathbf{x}) \right\|^2 \right).
\end{aligned} \tag{37}$$

Eq. (17).

$$\begin{cases} (\operatorname{tr}(\mathbf{S}))^2 \geq \operatorname{tr}(\mathbf{S}^2) & (\mathbf{S} \succ \mathbf{0}) \\ \operatorname{tr}(\mathbf{S}^2) \geq d^{-1} (\operatorname{tr}(\mathbf{S}))^2 & \text{(Jensen's inequality)} \end{cases} \quad (38)$$

$$\Rightarrow \operatorname{tr}(\mathbf{S}^2) \geq d^{-1} (\operatorname{tr}(\mathbf{S}))^2 \geq d^{-1} \operatorname{tr}(\mathbf{S}^2).$$

Eq. (19).

$$\begin{aligned} & \mathbb{E}_{\mathbf{y}, \varepsilon(\mathbf{T}\mathbf{y})} \left\| \mathbf{T}^{-1} \varepsilon(\mathbf{T}\mathbf{y}) \right\|^2 \\ &= \mathbb{E}_{\mathbf{y}, \boldsymbol{\eta}} \left\| \mathbf{T}^{-1} \operatorname{diag}(\boldsymbol{\eta}) \mathbf{T}\mathbf{y} \right\|^2 && \text{(Eq. (18))} \\ &= \mathbb{E}_{\mathbf{y}, \boldsymbol{\eta}} \mathbf{y}^\top \mathbf{T}^\top \operatorname{diag}(\boldsymbol{\eta}) \mathbf{T}^{-\top} \mathbf{T}^{-1} \operatorname{diag}(\boldsymbol{\eta}) \mathbf{T}\mathbf{y} \\ &= \mathbb{E}_{\mathbf{y}, \boldsymbol{\eta}} \operatorname{tr} \left(\mathbf{y}^\top \mathbf{T}^\top \operatorname{diag}(\boldsymbol{\eta}) \mathbf{T}^{-\top} \mathbf{T}^{-1} \operatorname{diag}(\boldsymbol{\eta}) \mathbf{T}\mathbf{y} \right) \\ &= \mathbb{E}_{\mathbf{y}, \boldsymbol{\eta}} \operatorname{tr} \left(\mathbf{T}^{-1} \operatorname{diag}(\boldsymbol{\eta}) \mathbf{T} \mathbf{y} \mathbf{y}^\top \mathbf{T}^\top \operatorname{diag}(\boldsymbol{\eta}) \mathbf{T}^{-\top} \right) \\ &= \operatorname{tr} \left(\mathbf{T}^{-1} \left(\mathbb{E}_{\boldsymbol{\eta}} \operatorname{diag}(\boldsymbol{\eta}) \mathbf{T} \left(\mathbb{E}_{\mathbf{y}} \mathbf{y} \mathbf{y}^\top \right) \mathbf{T}^\top \operatorname{diag}(\boldsymbol{\eta}) \right) \mathbf{T}^{-\top} \right) \\ &= \operatorname{tr} \left(\mathbf{T}^{-1} \left(\mathbb{E}_{\boldsymbol{\eta}} \operatorname{diag}(\boldsymbol{\eta}) \mathbf{U}' \mathbf{S}'^2 \mathbf{U}'^\top \operatorname{diag}(\boldsymbol{\eta}) \right) \mathbf{T}^{-\top} \right) && \text{(Eq. (36))} \\ &= \operatorname{tr} \left(\mathbf{T}^{-1} \left(\left(\mathbb{E}_{\boldsymbol{\eta}} \boldsymbol{\eta}^2 \right) \left(\mathbf{U}' \mathbf{S}'^2 \mathbf{U}'^\top \right) \odot \mathbf{I} \right) \mathbf{T}^{-\top} \right) \\ &= \left(\mathbb{E}_{\boldsymbol{\eta}} \boldsymbol{\eta}^2 \right) \operatorname{tr} \left(\mathbf{T}^{-1} \left(\left(\mathbf{U}' \mathbf{S}'^2 \mathbf{U}'^\top \right) \odot \mathbf{I} \right) \mathbf{T}^{-\top} \right). \end{aligned} \quad (39)$$

Eq. (20).

$$\begin{aligned}
& \text{tr} \left(\mathbf{T}^{-1} \left((\mathbf{U}' \mathbf{S}'^2 \mathbf{U}'^\top) \odot \mathbf{I} \right) \mathbf{T}^{-\top} \right) \\
&= \text{tr} \left(\mathbf{T}^{-1} \text{diag} \left(\|\mathbf{S}' \mathbf{U}'^\top \mathbf{e}_1\|^2, \dots, \|\mathbf{S}' \mathbf{U}'^\top \mathbf{e}_d\|^2 \right) \mathbf{T}^{-\top} \right) \\
&= \sum_{j=1}^d \sum_{k=1}^d (\mathbf{e}_j^\top \mathbf{T}^{-1} \mathbf{e}_k)^2 \|\mathbf{S}' \mathbf{U}'^\top \mathbf{e}_k\|^2 \\
&= \sum_{k=1}^d \|\mathbf{T}^{-1} \mathbf{e}_k\|^2 \|\mathbf{S}' \mathbf{U}'^\top \mathbf{e}_k\|^2 \\
&= \sum_{k=1}^d \|\mathbf{U} \mathbf{S} \mathbf{R} \mathbf{S}'^{-1} \mathbf{U}'^\top \mathbf{e}_k\|^2 \|\mathbf{S}' \mathbf{U}'^\top \mathbf{e}_k\|^2 && \text{(Eq. (16))} \\
&= \sum_{k=1}^d \|\mathbf{S} \mathbf{R} \mathbf{S}'^{-1} \mathbf{U}'^\top \mathbf{e}_k\|^2 \|\mathbf{R} \mathbf{S}' \mathbf{U}'^\top \mathbf{e}_k\|^2 && \text{(rotation-invariance of } L_2 \text{ norm) (40)} \\
&\geq \sum_{k=1}^d \left(\mathbf{e}_k^\top \mathbf{U}' \mathbf{S}'^{-1} \mathbf{R}^\top \mathbf{S} \mathbf{R} \mathbf{S}' \mathbf{U}'^\top \mathbf{e}_k \right)^2 && \text{(Cauchy-Schwarz)} \\
&= d \left(d^{-1} \sum_{k=1}^d \left(\mathbf{e}_k^\top \mathbf{U}' \mathbf{S}'^{-1} \mathbf{R}^\top \mathbf{S} \mathbf{R} \mathbf{S}' \mathbf{U}'^\top \mathbf{e}_k \right)^2 \right) \\
&\geq d \left(d^{-1} \sum_{k=1}^d \mathbf{e}_k^\top \mathbf{U}' \mathbf{S}'^{-1} \mathbf{R}^\top \mathbf{S} \mathbf{R} \mathbf{S}' \mathbf{U}'^\top \mathbf{e}_k \right)^2 && \text{(Jensen's inequality)} \\
&= d^{-1} \left(\text{tr} \left(\mathbf{U}' \mathbf{S}'^{-1} \mathbf{R}^\top \mathbf{S} \mathbf{R} \mathbf{S}' \mathbf{U}'^\top \right) \right)^2 \\
&= d^{-1} (\text{tr}(\mathbf{S}))^2.
\end{aligned}$$

The equality can be attained by choosing $\mathbf{U}' = \mathbf{H}$, $\mathbf{S}' = \mathbf{S}^{\frac{1}{2}}$, and $\mathbf{R} = \mathbf{I}$ such that

$$\begin{aligned}
& \text{tr} \left(\mathbf{T}^{-1} \left((\mathbf{U}' \mathbf{S}'^2 \mathbf{U}'^\top) \odot \mathbf{I} \right) \mathbf{T}^{-\top} \right) \\
&= \sum_{k=1}^d \left\| \mathbf{S} \mathbf{R} \mathbf{S}'^{-1} \mathbf{U}'^\top \mathbf{e}_k \right\|^2 \left\| \mathbf{R} \mathbf{S}' \mathbf{U}'^\top \mathbf{e}_k \right\|^2 \quad (\text{Eq. (40)}) \\
&= \sum_{k=1}^d \left(\left\| \mathbf{S}^{\frac{1}{2}} \mathbf{H}^\top \mathbf{e}_k \right\|^2 \right)^2 \quad (\text{plug in}) \\
&= \sum_{k=1}^d \left(\sum_{j=1}^d s_j \left(\mathbf{e}_j^\top \mathbf{H}^\top \mathbf{e}_k \right)^2 \right)^2 \\
&= \sum_{k=1}^d \left(\sum_{j=1}^d s_j d^{-1} \right)^2 \\
&= d \left(d^{-1} \sum_{j=1}^d s_j \right)^2 \\
&= d^{-1} (\text{tr}(\mathbf{S}))^2.
\end{aligned} \tag{41}$$

Eq. (21).

$$\begin{aligned}
& \mathbb{E}_{\mathbf{y}, \varepsilon(\mathbf{T}\mathbf{y})} \left\| \mathbf{T}^{-1} \varepsilon(\mathbf{T}\mathbf{y}) \right\|^2 \\
&= \mathbb{E}_{\mathbf{y}, \boldsymbol{\eta}} \left\| \mathbf{T}^{-1} \text{diag}(\boldsymbol{\eta}) \mathbf{T}\mathbf{y} \right\|^2 \quad (\text{Eq. (18)}) \\
&= \mathbb{E}_{\mathbf{y}, \boldsymbol{\eta}} \mathbf{y}^\top \mathbf{T}^\top \text{diag}(\boldsymbol{\eta}) \mathbf{T}^{-\top} \mathbf{T}^{-1} \text{diag}(\boldsymbol{\eta}) \mathbf{T}\mathbf{y} \\
&= \mathbb{E}_{\mathbf{y}, \boldsymbol{\eta}} \mathbf{y}^\top \mathbf{T}^\top \text{diag}(\boldsymbol{\eta})^2 \mathbf{T}\mathbf{y} \quad (\text{orthogonality of } \mathbf{T}) \\
&= \mathbb{E}_{\mathbf{y}} \mathbf{y}^\top \mathbf{T}^\top \left(\mathbb{E}_{\boldsymbol{\eta}} \text{diag}(\boldsymbol{\eta})^2 \right) \mathbf{T}\mathbf{y} \tag{42} \\
&= (\mathbb{E}_{\boldsymbol{\eta}} \boldsymbol{\eta}^2) \mathbb{E}_{\mathbf{y}} \mathbf{y}^\top \mathbf{T}^\top \mathbf{T}\mathbf{y} \\
&= (\mathbb{E}_{\boldsymbol{\eta}} \boldsymbol{\eta}^2) \mathbb{E}_{\mathbf{y}} \mathbf{y}^\top \mathbf{y} \quad (\text{orthogonality of } \mathbf{T}) \\
&= (\mathbb{E}_{\boldsymbol{\eta}} \boldsymbol{\eta}^2) \mathbb{E}_{\mathbf{y}} \|\mathbf{y}\|^2 \\
&= (\mathbb{E}_{\boldsymbol{\eta}} \boldsymbol{\eta}^2) \text{tr}(\mathbf{S}^2) \quad (\text{Eq. (36)}).
\end{aligned}$$

Eq. (22).

In the case of $\mathbf{U}' = \mathbf{I}$:

$$\begin{aligned}
& \text{tr} \left(\mathbf{T}^{-1} \left(\left(\mathbf{U}' \mathbf{S}'^2 \mathbf{U}'^\top \right) \odot \mathbf{I} \right) \mathbf{T}^{-\top} \right) \\
&= \text{tr} \left(\mathbf{U} \mathbf{S} \mathbf{R} \mathbf{S}'^{-1} \mathbf{U}'^\top \left(\left(\mathbf{U}' \mathbf{S}'^2 \mathbf{U}'^\top \right) \odot \mathbf{I} \right) \mathbf{U}' \mathbf{S}'^{-1} \mathbf{R}^\top \mathbf{S} \mathbf{U}^\top \right) \quad (\text{Eq. (16)}) \\
&= \text{tr} \left(\mathbf{U} \mathbf{S} \mathbf{R} \mathbf{S}'^{-1} \left(\mathbf{S}'^2 \odot \mathbf{I} \right) \mathbf{S}'^{-1} \mathbf{R}^\top \mathbf{S} \mathbf{U}^\top \right) \quad (\text{plug in}) \\
&= \text{tr} \left(\mathbf{U} \mathbf{S} \mathbf{R} \mathbf{S}'^{-1} \mathbf{S}'^2 \mathbf{S}'^{-1} \mathbf{R}^\top \mathbf{S} \mathbf{U}^\top \right) \quad (43) \\
&= \text{tr} \left(\mathbf{U} \mathbf{S} \mathbf{R} \mathbf{R}^\top \mathbf{S} \mathbf{U}^\top \right) \\
&= \text{tr} \left(\mathbf{U} \mathbf{S}^2 \mathbf{U}^\top \right) \\
&= \text{tr} \left(\mathbf{S}^2 \right).
\end{aligned}$$

In the case of $\mathbf{S}' = \mathbf{I}$:

$$\begin{aligned}
& \text{tr} \left(\mathbf{T}^{-1} \left(\left(\mathbf{U}' \mathbf{S}'^2 \mathbf{U}'^\top \right) \odot \mathbf{I} \right) \mathbf{T}^{-\top} \right) \\
&= \text{tr} \left(\mathbf{U} \mathbf{S} \mathbf{R} \mathbf{S}'^{-1} \mathbf{U}'^\top \left(\left(\mathbf{U}' \mathbf{S}'^2 \mathbf{U}'^\top \right) \odot \mathbf{I} \right) \mathbf{U}' \mathbf{S}'^{-1} \mathbf{R}^\top \mathbf{S} \mathbf{U}^\top \right) \quad (\text{Eq. (16)}) \\
&= \text{tr} \left(\mathbf{U} \mathbf{S} \mathbf{R} \mathbf{U}'^\top \left(\left(\mathbf{U}' \mathbf{U}'^\top \right) \odot \mathbf{I} \right) \mathbf{U}' \mathbf{R}^\top \mathbf{S} \mathbf{U}^\top \right) \quad (\text{plug in}) \\
&= \text{tr} \left(\mathbf{U} \mathbf{S} \mathbf{R} \mathbf{U}'^\top \mathbf{U}' \mathbf{R}^\top \mathbf{S} \mathbf{U}^\top \right) \quad (44) \\
&= \text{tr} \left(\mathbf{U} \mathbf{S}^2 \mathbf{U}^\top \right) \\
&= \text{tr} \left(\mathbf{S}^2 \right).
\end{aligned}$$

Eq. (24).

$$\begin{aligned}
& \mathbb{E}_{\mathbf{y}, \varepsilon(\mathbf{T}\mathbf{y})} \left\| \mathbf{T}^{-1} \varepsilon(\mathbf{T}\mathbf{y}) \right\|^2 \\
&= \mathbb{E}_{\mathbf{y}, \boldsymbol{\eta}} \left\| \mathbf{T}^{-1} \left\| \mathbf{T}\mathbf{y} \right\|_\infty \boldsymbol{\eta} \right\|^2 \quad (\text{Eq. (23)}) \\
&= \mathbb{E}_{\mathbf{y}, \boldsymbol{\eta}} \left\| \mathbf{T}\mathbf{y} \right\|_\infty^2 \boldsymbol{\eta}^\top \mathbf{T}^{-\top} \mathbf{T}^{-1} \boldsymbol{\eta} \\
&= \mathbb{E}_{\mathbf{y}, \boldsymbol{\eta}} \left\| \mathbf{T}\mathbf{y} \right\|_\infty^2 \text{tr} \left(\boldsymbol{\eta}^\top \mathbf{T}^{-\top} \mathbf{T}^{-1} \boldsymbol{\eta} \right) \\
&= \mathbb{E}_{\mathbf{y}, \boldsymbol{\eta}} \left\| \mathbf{T}\mathbf{y} \right\|_\infty^2 \text{tr} \left(\mathbf{T}^{-1} \boldsymbol{\eta} \boldsymbol{\eta}^\top \mathbf{T}^{-\top} \right) \quad (45) \\
&= \text{tr} \left(\mathbf{T}^{-1} \left(\mathbb{E}_{\boldsymbol{\eta}} \boldsymbol{\eta} \boldsymbol{\eta}^\top \right) \mathbf{T}^{-\top} \right) \mathbb{E}_{\mathbf{y}} \left\| \mathbf{T}\mathbf{y} \right\|_\infty^2 \\
&= \left(\mathbb{E}_{\boldsymbol{\eta}} \boldsymbol{\eta}^2 \right) \text{tr} \left(\mathbf{T}^{-1} \mathbf{T}^{-\top} \right) \mathbb{E}_{\mathbf{y}} \left\| \mathbf{T}\mathbf{y} \right\|_\infty^2 \\
&= \left(\mathbb{E}_{\boldsymbol{\eta}} \boldsymbol{\eta}^2 \right) \left\| \mathbf{T}^{-1} \right\|_{\text{F}}^2 \mathbb{E}_{\mathbf{y}} \left\| \mathbf{T}\mathbf{y} \right\|_\infty^2.
\end{aligned}$$

Eq. (25).

$$\begin{aligned}
\|\mathbf{T}^{-1}\|_{\text{F}}^2 &= \text{tr}(\mathbf{T}^{-1}\mathbf{T}^{-\top}) \\
&= \text{tr}(\mathbf{U}\mathbf{S}\mathbf{R}\mathbf{S}'^{-1}\mathbf{U}'^{\top}\mathbf{U}'\mathbf{S}'^{-1}\mathbf{R}^{\top}\mathbf{S}\mathbf{U}^{\top}) \quad (\text{Eq. (16)}) \\
&= \text{tr}(\mathbf{S}\mathbf{U}^{\top}\mathbf{U}\mathbf{S}\mathbf{R}\mathbf{S}'^{-1}\mathbf{U}'^{\top}\mathbf{U}'\mathbf{S}'^{-1}\mathbf{R}^{\top}) \\
&= \text{tr}(\mathbf{S}^2\mathbf{R}\mathbf{S}'^{-2}\mathbf{R}^{\top})
\end{aligned} \tag{46}$$

Because $s_1^2 \geq \dots \geq s_d^2$ and $s_1'^{-2} \leq \dots \leq s_d'^{-2}$, using von Neumann's trace inequality,

$$\|\mathbf{T}^{-1}\|_{\text{F}}^2 = \text{tr}(\mathbf{S}^2\mathbf{R}\mathbf{S}'^{-2}\mathbf{R}^{\top}) \geq \text{tr}(\mathbf{S}^2\mathbf{S}'^{-2}). \tag{47}$$

The equality can be attained by choosing $\mathbf{R} = \mathbf{I}$.

Eq. (26).

Express the expectations as

$$\mathbb{E}_{\mathbf{y}} \|\mathbf{T}\mathbf{y}\|_{\infty}^2 = \mathbb{E}_{\mathbf{y}} \max_k (\mathbf{e}_k^{\top}\mathbf{T}\mathbf{y})^2 \geq \max_k \mathbb{E}_{\mathbf{y}} (\mathbf{e}_k^{\top}\mathbf{T}\mathbf{y})^2 \quad (\text{Jensen's inequality}) \tag{48}$$

and

$$\mathbb{E}_{\mathbf{y}} \|\mathbf{T}\mathbf{y}\|^2 = \mathbb{E}_{\mathbf{y}} \sum_{k=1}^d (\mathbf{e}_k^{\top}\mathbf{T}\mathbf{y})^2 = \sum_{k=1}^d \mathbb{E}_{\mathbf{y}} (\mathbf{e}_k^{\top}\mathbf{T}\mathbf{y})^2. \tag{49}$$

By the relationships among the mean, maximum, and summation values, we have:

$$d^{-1}\mathbb{E}_{\mathbf{y}} \|\mathbf{T}\mathbf{y}\|^2 \leq \max_k \mathbb{E}_{\mathbf{y}} (\mathbf{e}_k^{\top}\mathbf{T}\mathbf{y})^2 \leq \mathbb{E}_{\mathbf{y}} \|\mathbf{T}\mathbf{y}\|_{\infty}^2 \leq \mathbb{E}_{\mathbf{y}} \|\mathbf{T}\mathbf{y}\|^2 \leq d \max_k \mathbb{E}_{\mathbf{y}} (\mathbf{e}_k^{\top}\mathbf{T}\mathbf{y})^2, \tag{50}$$

where, by Eq. (36),

$$\mathbb{E}_{\mathbf{y}} \|\mathbf{T}\mathbf{y}\|^2 = \text{tr}(\mathbf{S}'^2) \tag{51}$$

and

$$\mathbb{E}_{\mathbf{y}} (\mathbf{e}_k^{\top}\mathbf{T}\mathbf{y})^2 = \mathbf{e}_k^{\top}\mathbf{T}(\mathbb{E}_{\mathbf{y}}\mathbf{y}\mathbf{y}^{\top})\mathbf{T}^{\top}\mathbf{e}_k = \mathbf{e}_k^{\top}\mathbf{U}'\mathbf{S}'^2\mathbf{U}'^{\top}\mathbf{e}_k = \left\| \mathbf{S}'\mathbf{U}'^{\top}\mathbf{e}_k \right\|^2. \tag{52}$$

Lemma 3 (Maximum Inequalities for Tail-Bounded Distributions) *If $X_1, \dots, X_d \in \mathbb{R}$ are zero-mean Gaussian random variables,*

$$\mathbb{E} \max_k X_k^2 \leq \min\{d, (2 \ln(2d) + 2)\} \max_k \mathbb{E} X_k^2. \tag{53}$$

If $X_1, \dots, X_d \in \mathbb{R}$ are zero-mean Laplacian random variables,

$$\mathbb{E} \max_k X_k^2 \leq (2^{-1}(\ln d)^2 + \ln d + 1) \max_k \mathbb{E} X_k^2. \tag{54}$$

Both inequalities hold without the need for independence.

Proof We provide proofs for the Gaussian and Laplacian distributions in Sections [A.5.1](#) and [A.5.2](#), respectively. \blacksquare

Using Lemma 3, for a tail-bounded \mathcal{D}_y that is a zero-mean multivariate Gaussian or Laplacian, we can further tighten the upper bound by

$$\mathbb{E}_y \|\mathbf{T}\mathbf{y}\|_\infty^2 \leq \min \left\{ d^{o(1)} \max_k \mathbb{E}_y \left(\mathbf{e}_k^\top \mathbf{T}\mathbf{y} \right)^2, \mathbb{E}_y \|\mathbf{T}\mathbf{y}\|^2 \right\}. \quad (55)$$

When $\mathbf{U}' = \mathbf{H}$, using Eqs. (36), (52), the marginal second moment in Eq. (55) becomes

$$\begin{aligned} \mathbb{E}_y \left(\mathbf{e}_k^\top \mathbf{T}\mathbf{y} \right)^2 &= \left\| \mathbf{S}'\mathbf{U}'^\top \mathbf{e}_k \right\|^2 = \left\| \mathbf{S}'\mathbf{H}^\top \mathbf{e}_k \right\|^2 = \sum_{j=1}^d s_j'^2 d^{-1} = d^{-1} \text{tr}(\mathbf{S}'^2) \\ &= d^{-1} \mathbb{E}_y \|\mathbf{T}\mathbf{y}\|^2, \end{aligned} \quad (56)$$

which is equalized for all k , and $\max_k \mathbb{E}_y \left(\mathbf{e}_k^\top \mathbf{T}\mathbf{y} \right)^2$ is minimized to $d^{-1} \mathbb{E}_y \|\mathbf{T}\mathbf{y}\|^2$. Finally, combining Eqs. (50), (55), (56),

$$d^{-1} \text{tr}(\mathbf{S}'^2) \leq \mathbb{E}_y \|\mathbf{T}\mathbf{y}\|_\infty^2 \leq \begin{cases} d^{o(1)-1} \text{tr}(\mathbf{S}'^2), & \text{tail-bounded } \mathcal{D}_y, \\ \text{tr}(\mathbf{S}'^2), & \text{otherwise.} \end{cases} \quad (57)$$

Eq. (31).

For orthogonal \mathbf{T} , we have $\|\mathbf{T}^{-1}\|_F^2 = d$ and $\mathbb{E}_y \|\mathbf{T}\mathbf{y}\|^2 = \mathbb{E}_y \|\mathbf{y}\|^2$. Using Eq. (36), $\mathbb{E}_y \|\mathbf{y}\|^2 = \text{tr}(\mathbf{S}^2)$. By Eq. (50),

$$\begin{aligned} \text{tr}(\mathbf{S}^2) &= d^{-1} \|\mathbf{T}^{-1}\|_F^2 \mathbb{E}_y \|\mathbf{T}\mathbf{y}\|^2 \\ &\leq \|\mathbf{T}^{-1}\|_F^2 \mathbb{E}_y \|\mathbf{T}\mathbf{y}\|_\infty^2 \leq \|\mathbf{T}^{-1}\|_F^2 \mathbb{E}_y \|\mathbf{T}\mathbf{y}\|^2 = d \text{tr}(\mathbf{S}^2). \end{aligned} \quad (58)$$

A.4 Quantization Error Modeling Justifications

A.4.1 INTEGER (INT) TYPES

We model the quantization error using pseudo noise similar to DiffQ ([Défossez et al., 2022](#)).

Define the scalar quantizer of b -bit symmetric integer as

$$q(x) = (\lfloor xs^{-1} \rfloor + 2^{-1}) s, \quad (59)$$

where $x \in \mathbb{R}$, scale $s \in \mathbb{R}_{\neq 0}$, and $xs^{-1} \in [-2^{b-1}, 2^{b-1})$.

To simplify the analysis, we model the quantizer as

$$q(x) = (xs^{-1} + \xi) s = x + s\xi \quad (60)$$

with random noise $\xi \sim \text{Uniform}(-2^{-1}, 2^{-1})$. Then, the quantization error can be expressed as

$$q(x) - x = s\xi. \quad (61)$$

For a vector $\boldsymbol{\alpha} \in \mathbb{R}^d$, we use the AbsMax scale $s = 2^{1-b} \|\boldsymbol{\alpha}\|_\infty$. Define

$$\eta = 2^{1-b} \xi, \quad (62)$$

then we have $s\xi = \eta \|\boldsymbol{\alpha}\|_\infty$. The quantization error of vector $\boldsymbol{\alpha}$ is

$$\varepsilon(\boldsymbol{\alpha}) = \|\boldsymbol{\alpha}\|_\infty \boldsymbol{\eta} \quad (63)$$

with $\boldsymbol{\eta} = [\eta_1, \dots, \eta_d]^\top \in \mathbb{R}^d$ being a random vector of i.i.d. samples $\eta \sim \mathcal{D}_\eta$ and

$$\mathbb{E}_\eta \boldsymbol{\eta} = 2^{1-b} \mathbb{E}_\xi \boldsymbol{\xi} = \mathbf{0} \quad (64)$$

A.4.2 FLOATING-POINT (FP) TYPES

The FP format $EaMb$ is defined as a tuple (s, e, m) with a sign $s \in \{0, 1\}$, an exponent $e \in \{0, \dots, 2^a - 1\}$, and a mantissa $m \in \{0, \dots, 2^b - 1\}$. Assume we do not need to consider the subnormal and special number cases. The tuple (s, e, m) represents the number

$$x_{EaMb} = (-1)^s 2^{e-2^{a-1}+1} \left(1 + 2^{-b}m\right). \quad (65)$$

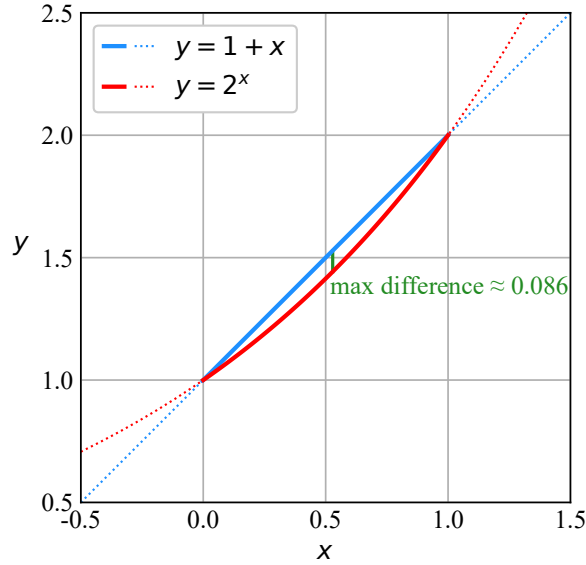


Figure 5: The two curves $y = 1 + x$ and $y = 2^x$ are close for $0 \leq x \leq 1$.

Using the approximation $1 + (\cdot) \approx 2^{(\cdot)}$ for $2^{-b}m \in [0, 1]$ (visualized in Figure 5), we define a smoothed version of $EaMb$, named $SEaMb$, as

$$x_{SEaMb} = (-1)^s 2^{e-2^{a-1}+1} 2^{2^{-b}m} = (-1)^s 2^{2^{-b}(2^b e + m) - 2^{a-1} + 1} \quad (66)$$

with

$$2^b e + m = 2^b (\log_2 |x_{SEaMb}| + 2^{a-1} - 1) \quad (67)$$

being an $(a + b)$ -bit unsigned integer (concatenating the binary representations of e and m). The minimum and maximum of $|x_{\text{SEaMb}}|$ are

$$\begin{aligned}\min |x_{\text{SEaMb}}| &= 2^{-2^{a-1}+1}, \\ \max |x_{\text{SEaMb}}| &= 2^{2^{-b}(2^{a+b}-1)-2^{a-1}+1} = 2^{2^{a-1}-2^{-b}+1},\end{aligned}\tag{68}$$

respectively.

Denote $\text{SEaMb}(x)$ as the quantizer that casts $x \in [-\max |x_{\text{SEaMb}}|, \max |x_{\text{SEaMb}}|]$ to the nearest number in the SEaMb type. Assume $e \in (-\infty, 2^a - 1]$ so that the smaller values can be represented more precisely. $\text{SEaMb}(x)$ can be approximated using integer rounding in logarithmic space and first-order expansion. For $x \neq 0$,

$$\begin{aligned}\text{SEaMb}(x) &\approx \text{sgn}(x) 2^{2^{-b} \lceil 2^b (\log_2 |x| + 2^{a-1} - 1) \rceil - 2^{a-1} + 1} \\ &= \text{sgn}(x) 2^{2^{-b} \lceil 2^b \log_2 |x| \rceil} \\ &\approx \text{sgn}(x) \left(2^{2^{-b} 2^b \log_2 |x|} + \left(\lceil 2^b \log_2 |x| \rceil - 2^b \log_2 |x| \right) 2^{2^{-b} 2^b \log_2 |x|} 2^{-b \ln 2} \right) \\ &= x \left(1 + \left(\lceil 2^b \log_2 |x| \rceil - 2^b \log_2 |x| \right) 2^{-b \ln 2} \right).\end{aligned}\tag{69}$$

For $x = 0$,

$$\text{SEaMb}(0) \approx \lim_{x \rightarrow 0} x \left(1 + \left(\lceil 2^b \log_2 |x| \rceil - 2^b \log_2 |x| \right) 2^{-b \ln 2} \right) = 0.\tag{70}$$

We model the casting error as

$$\text{SEaMb}(x) - x = (\ln 2) 2^{-b} \xi x\tag{71}$$

where $x \in [-\max |x_{\text{SEaMb}}|, \max |x_{\text{SEaMb}}|]$ and, similar to the INT types in Eq. (60), the random variable $\xi \sim \text{Uniform}(-2^{-1}, 2^{-1})$.

For a quantization format that uses EaMb for values and $\text{E}\tilde{\text{a}}\tilde{\text{M}}\tilde{\text{b}}$ for scales, we approximate it with a scalar quantizer $q(x) = \text{SEaMb}(xs^{-1}) \text{SE}\tilde{\text{a}}\tilde{\text{M}}\tilde{\text{b}}(s)$ where $x \in \mathbb{R}$, scale $s \in \mathbb{R}_{\neq 0}$, $|s| \leq \max |x_{\text{SE}\tilde{\text{a}}\tilde{\text{M}}\tilde{\text{b}}}|$, and $|xs^{-1}| \leq \max |x_{\text{SEaMb}}|$. Then,

$$\begin{aligned}q(x) &= \text{SEaMb}(xs^{-1}) \text{SE}\tilde{\text{a}}\tilde{\text{M}}\tilde{\text{b}}(s) \\ &= \left(1 + (\ln 2) 2^{-b} \xi \right) xs^{-1} \left(1 + (\ln 2) 2^{-\tilde{b}} \tilde{\xi} \right) s \\ &= \left(1 + (\ln 2) 2^{-b} \xi \right) \left(1 + (\ln 2) 2^{-\tilde{b}} \tilde{\xi} \right) x\end{aligned}\tag{72}$$

with the independent random variables $\xi, \tilde{\xi} \sim \text{Uniform}(-2^{-1}, 2^{-1})$.

Define

$$\eta = \left(1 + (\ln 2) 2^{-b} \xi \right) \left(1 + (\ln 2) 2^{-\tilde{b}} \tilde{\xi} \right) - 1.\tag{73}$$

Then, the quantization error can be expressed as

$$q(x) - x = \eta x.\tag{74}$$

And the expected quantization error is 0 because

$$\mathbb{E}_\eta \eta = \mathbb{E}_{\xi, \tilde{\xi}} (\ln 2) 2^{-b} \xi + (\ln 2) 2^{-\tilde{b}} \tilde{\xi} + (\ln 2)^2 2^{-b-\tilde{b}} \xi \tilde{\xi} = 0.\tag{75}$$

A.5 Maximum Inequalities for Tail-Bounded Distributions

Lemma 4 (Expectation from the Survival Function) *Let $X \geq 0$ be a random variable with the density function f and the survival function*

$$S(t) = \mathbb{P}(X \geq t) \tag{76}$$

with $t \geq 0$. Let $g : [0, \infty) \rightarrow \mathbb{R}$ be integrable and define

$$G(t) = \int_0^t g(u) \, du. \tag{77}$$

Assume that

$$\lim_{t \rightarrow \infty} G(t) S(t) = 0. \tag{78}$$

Then,

$$\mathbb{E}G(X) = \int_0^\infty g(t) S(t) \, dt. \tag{79}$$

Proof Since X has density f and takes values in $[0, \infty)$,

$$\mathbb{E}G(X) = \int_0^\infty G(t) f(t) \, dt. \tag{80}$$

The survival function satisfies

$$S(t) = \mathbb{P}(X \geq t) = \int_t^\infty f(u) \, du, \tag{81}$$

so S is differentiable almost everywhere with $S'(t) = -f(t)$. Hence,

$$\mathbb{E}G(X) = \int_0^\infty G(t) f(t) \, dt = - \int_0^\infty G(t) S'(t) \, dt. \tag{82}$$

We now integrate by parts, using $G'(t) = g(t)$,

$$- \int_0^\infty G(t) S'(t) \, dt = - [G(t) S(t)]_0^\infty + \int_0^\infty g(t) S(t) \, dt. \tag{83}$$

By definition, $G(0) = 0$, and by assumption $\lim_{t \rightarrow \infty} G(t) S(t) = 0$, the boundary term $[G(t) S(t)]_0^\infty = 0$. Therefore,

$$\mathbb{E}G(X) = \int_0^\infty g(t) S(t) \, dt. \tag{84}$$

■

A.5.1 GAUSSIAN DISTRIBUTION

Definition of sub-Gaussian.

A probability distribution of a random variable $X \in \mathbb{R}$ is called sub-Gaussian with variance proxy σ^2 if

$$\mathbb{E} \exp((X - \mathbb{E}X) t) \leq \exp(2^{-1} \sigma^2 t^2) \quad (85)$$

for all $t \in \mathbb{R}$, and the smallest such σ^2 is called the optimal variance proxy.

Basic properties of sub-Gaussian distributions.

The variance proxy is larger than or equal to the variance: $\sigma^2 \geq \mathbb{E}(X - \mathbb{E}X)^2$. For a Gaussian distribution, the optimal variance proxy is the same as the variance.

Chernoff bound on the tail:

$$\mathbb{P}(|X - \mathbb{E}X| \geq t) \leq 2 \exp(-2^{-1} \sigma^{-2} t^2) \quad (86)$$

for all $t \geq 0$.

Maximum inequality.

Let X_1, \dots, X_d be zero-mean Gaussian random variables with variance $\sigma_1^2, \dots, \sigma_d^2$. Denote

$$\sigma_\star^2 = \max_k \sigma_k^2 = \max_k \mathbb{E}X_k^2 \quad (87)$$

as the smallest variance proxy for X_1, \dots, X_d . Using Lemma 4,

$$\begin{aligned} \mathbb{E} \max_k X_k^2 &= 2 \int_0^\infty t \mathbb{P}\left(\max_k |X_k| \geq t\right) dt \\ &= 2 \int_0^\infty t \mathbb{P}\left(\bigcup_{k=1}^d \{|X_k| \geq t\}\right) dt \\ &\leq 2 \int_0^{t_\star} t \, 1 \, dt + 2 \int_{t_\star}^\infty t \left(\sum_{k=1}^d \mathbb{P}(|X_k| \geq t)\right) dt \\ &\leq 2 \int_0^{t_\star} t \, dt + 2d \int_{t_\star}^\infty t \left(\max_k \mathbb{P}(|X_k| \geq t)\right) dt \\ &\leq 2 \int_0^{t_\star} t \, dt + 4d \int_{t_\star}^\infty t \exp(-2^{-1} \sigma_\star^{-2} t^2) dt \\ &= [t^2]_0^{t_\star} + 4d [-\sigma_\star^2 \exp(-2^{-1} \sigma_\star^{-2} t^2)]_{t_\star}^\infty \\ &= t_\star^2 + 4d \sigma_\star^2 \exp(-2^{-1} \sigma_\star^{-2} t_\star^2). \end{aligned} \quad (88)$$

Splitting at $t_\star = \sigma_\star \sqrt{2 \ln(2d)}$ gives

$$\mathbb{E} \max_k X_k^2 \leq 2\sigma_\star^2 \ln(2d) + 2\sigma_\star^2 = (2 \ln(2d) + 2) \max_k \mathbb{E}X_k^2 \quad (89)$$

without needing the independence of X_k . Also, considering the trivial bound

$$\mathbb{E} \max_k X_k^2 \leq \mathbb{E} \sum_{k=1}^d X_k^2 = \sum_{k=1}^d \mathbb{E}X_k^2 \leq d \max_k \mathbb{E}X_k^2, \quad (90)$$

then,

$$\mathbb{E} \max_k X_k^2 \leq \min \{d, (2 \ln(2d) + 2)\} \max_k \mathbb{E} X_k^2. \quad (91)$$

A.5.2 LAPLACIAN DISTRIBUTION

For a random variable $X \sim \text{Laplace}(\mu, b)$ and $t \geq 0$,

$$\mathbb{P}(|X - \mu| \geq t) = 2 \int_t^\infty 2^{-1} b^{-1} \exp(-b^{-1}x) dx = \exp(-b^{-1}t). \quad (92)$$

The variance $\mathbb{E}(X - \mathbb{E}X)^2 = 2b^2$.

Let X_1, \dots, X_d be zero-mean Laplacian random variables with diversity b_1, \dots, b_d . Denote

$$b_\star = \max_k b_k = \max_k \sqrt{\frac{1}{2} \mathbb{E} X_k^2} = \sqrt{\frac{1}{2} \max_k \mathbb{E} X_k^2}. \quad (93)$$

For $t \geq 0$,

$$\mathbb{P}(|X_k| \geq t) = \exp(-b_k^{-1}t) \leq \exp(-b_\star^{-1}t). \quad (94)$$

Using Lemma 4,

$$\begin{aligned} \mathbb{E} \max_k X_k^2 &= 2 \int_0^\infty t \mathbb{P}\left(\max_k |X_k| \geq t\right) dt \\ &= 2 \int_0^\infty t \mathbb{P}\left(\bigcup_{k=1}^d \{|X_k| \geq t\}\right) dt \\ &\leq 2 \int_0^{t_\star} t \, 1 \, dt + 2 \int_{t_\star}^\infty t \left(\sum_{k=1}^d \mathbb{P}(|X_k| \geq t)\right) dt \\ &\leq 2 \int_0^{t_\star} t \, dt + 2d \int_{t_\star}^\infty t \left(\max_k \mathbb{P}(|X_k| \geq t)\right) dt \\ &\leq 2 \int_0^{t_\star} t \, dt + 2d \int_{t_\star}^\infty t \exp(-b_\star^{-1}t) dt \\ &= [t^2]_0^{t_\star} + 2d [-b_\star(t + b_\star) \exp(-b_\star^{-1}t)]_{t_\star}^\infty \\ &= t_\star^2 + 2db_\star(t_\star + b_\star) \exp(-b_\star^{-1}t_\star). \end{aligned} \quad (95)$$

Splitting at $t_\star = b_\star \ln d$ gives

$$\mathbb{E} \max_k X_k^2 \leq b_\star^2 \left((\ln d)^2 + 2 \ln d + 2 \right) = \left(2^{-1} (\ln d)^2 + \ln d + 1 \right) \max_k \mathbb{E} X_k^2 \quad (96)$$

without needing the independence of X_k .

Appendix B. Further Experimental Results

In this section, we report additional evaluations conducted across the Llama 3 and Qwen 3 family models in Tables 3 and 4 and Figures 6 to 9. For the Qwen models, the thinking mode is disabled across all experiments. The evaluation results are obtained using emulated (“fake”) quantization, where quantized values are represented in the BF16/FP16 format. Results are aggregated over multiple random seeds.

Table 3: KL-divergence for Qwen3-8B measured on a slice of C4 dataset, with calibration performed on FineWeb dataset. Results (lower is better) are averaged over multiple random seeds. H denotes the Hadamard transform.

Model	Format	Quantization	Transform	KL
Qwen3-8B	NVFP4	GPTQ	H	0.069518
		RTN	WUSH	0.065747
		GPTQ	WUSH	0.054646
	MXFP4	GPTQ	H	0.093119
		RTN	WUSH	0.093739
		GPTQ	WUSH	0.077909

Table 4: W4A4 accuracy results on the LM Evaluation Harness for different models with RTN, GPTQ quantizations, and identity (I), Hadamard (H), WUSH transforms. For the Llama model, the MMLU-CoT metric is reported in the MMLU column.

Model	Format	Quantization	Transform	MMLU	GSM8K	HellaSwag	WinoGrande	Average	Recovery
Llama-3.2-3B-Instruct	BF16	-	-	64.43	78.01	73.42	70.09	71.49	100.0
	NVFP4	RTN	I	61.07	72.01	70.90	66.77	67.69	94.68
			H	59.91	64.82	69.77	65.59	65.02	90.95
		GPTQ	WUSH	59.91	71.24	70.96	67.25	67.34	94.19
			H	60.22	70.91	71.06	66.57	67.19	93.99
	MXFP4	RTN	WUSH	60.17	72.71	71.26	67.32	67.87	94.93
			I	56.81	60.80	67.30	64.56	62.37	87.24
		GPTQ	H	55.99	61.11	68.36	64.09	62.39	87.27
WUSH			59.54	69.49	70.20	66.47	66.43	92.92	
Qwen3-8B	BF16	-	-	72.98	90.90	75.52	70.56	77.49	100.0
	NVFP4	RTN	I	70.47	88.40	74.44	69.53	75.71	97.70
			H	70.19	86.35	73.02	68.11	74.42	96.04
		GPTQ	WUSH	70.86	89.92	74.84	70.02	76.42	98.61
			H	70.78	89.11	74.34	69.25	75.87	97.91
	MXFP4	RTN	WUSH	71.03	89.56	74.88	70.32	76.45	98.66
			I	67.69	84.23	71.24	67.40	72.64	93.74
		GPTQ	H	67.53	87.04	71.48	67.64	73.42	94.75
WUSH			69.96	86.90	73.87	68.92	74.91	96.68	
Qwen3-14B	BF16	-	-	77.18	91.96	79.84	74.27	80.81	100.0
	NVFP4	RTN	I	75.20	90.22	77.38	73.32	79.03	97.80
			H	74.98	92.04	77.76	72.38	79.29	98.12
		GPTQ	WUSH	75.43	91.78	78.82	73.18	79.80	98.76
			I	72.92	90.22	76.68	71.51	77.83	96.31
	MXFP4	RTN	H	73.13	87.41	76.29	71.67	77.13	95.44
			WUSH	74.56	91.87	78.18	73.15	79.44	98.30
	Qwen3-32B	BF16	-	-	80.74	92.12	83.96	76.95	83.44
NVFP4		RTN	I	78.92	90.14	82.60	76.64	82.08	98.37
			H	79.48	91.81	82.51	74.98	82.20	98.51
		GPTQ	WUSH	79.56	92.72	83.14	75.79	82.80	99.24
			I	76.82	75.28	81.32	74.74	77.04	92.33
MXFP4		RTN	H	78.63	92.57	81.87	75.53	82.15	98.45
			WUSH	78.70	90.83	82.63	75.87	82.01	98.28

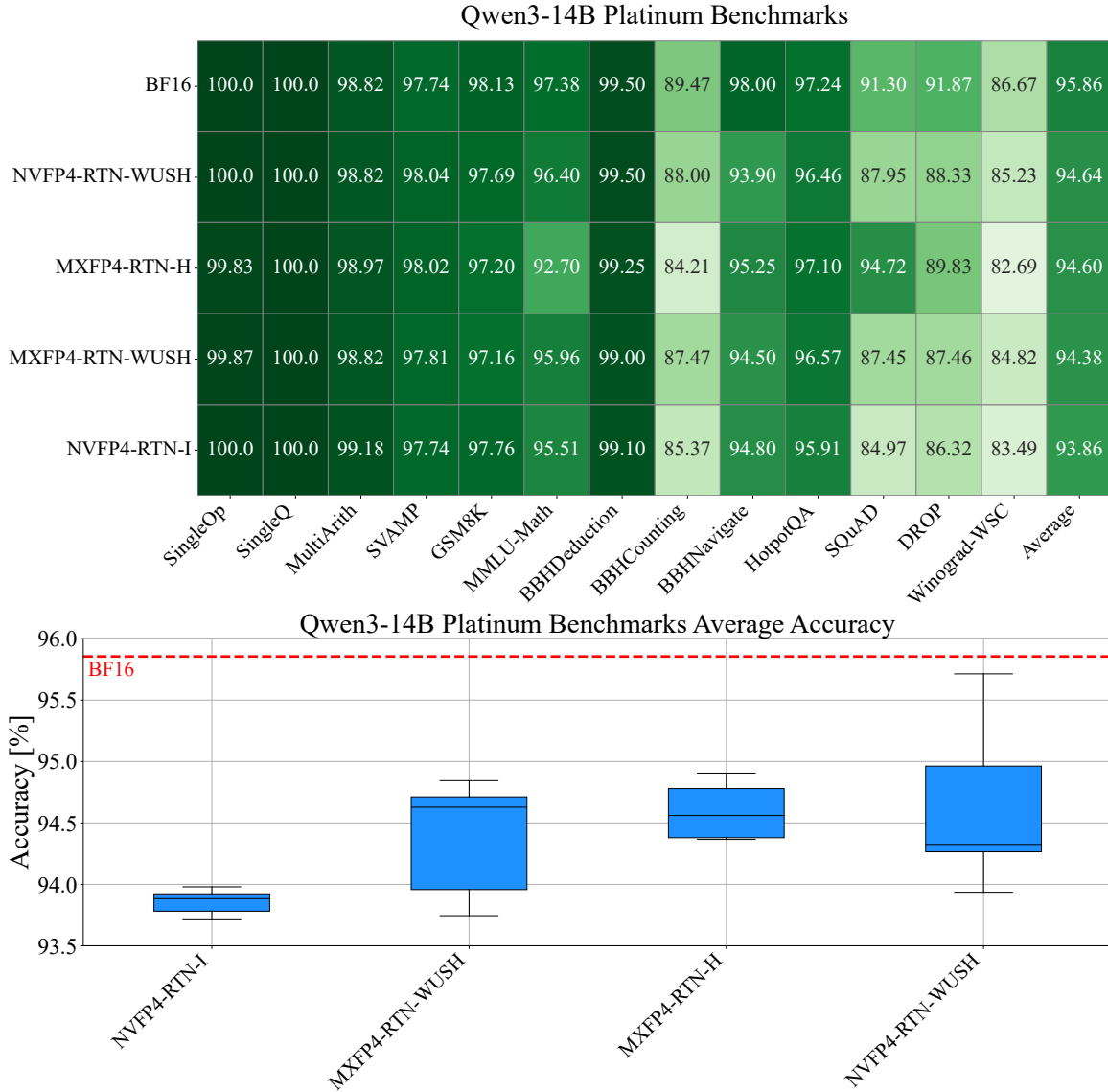


Figure 6: Comparison of different transforms on Qwen3-14B for both NVFP4 and MXFP4 RTN quantization on Platinum Benchmarks. The top table shows accuracy results across the individual benchmark tasks, while the bottom plot shows the average accuracy scores together with their standard deviations for each transform.

Qwen3-32B Platinum Benchmarks

BF16	100.0	100.0	99.41	97.36	98.88	94.01	100.0	95.26	98.00	99.45	95.03	94.74	93.85	97.38
NVFP4-RTN-H	99.67	100.0	98.97	99.06	98.13	95.32	99.75	91.18	97.88	97.79	93.32	93.54	92.44	96.70
NVFP4-RTN-WUSH	99.83	100.0	98.82	97.92	98.13	95.60	99.50	91.32	97.25	98.07	93.01	93.42	92.69	96.58
MXFP4-RTN-WUSH	99.33	100.0	99.12	98.58	97.76	95.51	99.12	90.66	97.75	98.62	93.79	92.82	91.15	96.48
NVFP4-RTN-I	100.0	100.0	99.41	98.58	98.69	94.48	99.75	86.84	97.25	98.34	92.86	94.38	92.31	96.38
MXFP4-RTN-H	99.33	100.0	98.24	97.26	97.76	93.63	99.25	81.18	96.50	98.48	93.01	92.58	90.90	95.24
MXFP4-RTN-I	100.0	100.0	99.26	98.40	97.67	92.51	99.25	85.26	94.75	97.38	91.77	90.43	90.64	95.18
	SingleOp	SingleQ	MultiArith	SVAMP	GSM8K	MMLU-Math	BBH Deduction	BBH Counting	BBH Navigate	HotpotQA	SQuAD	DROP	Winograd-WSC	Average

Qwen3-32B Platinum Benchmarks Average Accuracy

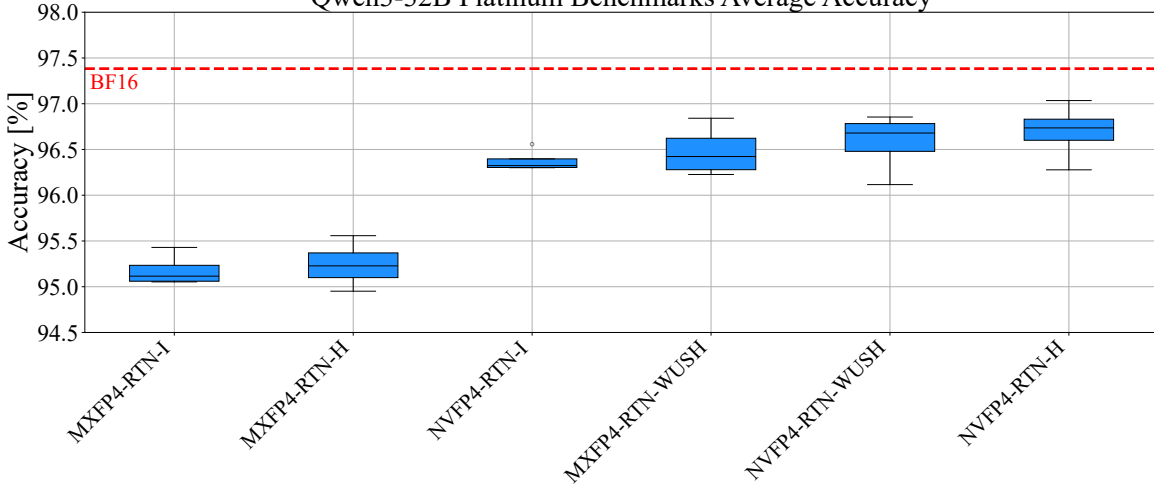


Figure 7: Comparison of different transforms on Qwen3-32B for both NVFP4 and MXFP4 RTN quantization on Platinum Benchmarks. The top table shows accuracy results across the individual benchmark tasks, while the bottom plot shows the average accuracy scores together with their standard deviations for each transform.

Llama-3.2-3B-Instruct Platinum Benchmarks

BF16	98.67	98.00	99.41	91.32	84.70	62.55	73.50	78.95	63.50	81.22	79.50	53.59	63.59	79.11
NVFP4-GPTQ-I	97.20	98.80	96.82	87.77	79.25	58.73	66.80	68.74	65.30	79.45	71.80	53.68	62.56	75.92
NVFP4-GPTQ-WUSH	96.80	98.80	96.59	86.49	79.55	57.15	64.50	69.47	62.90	75.58	73.29	52.92	62.36	75.11
NVFP4-GPTQ-H	97.33	98.80	96.24	87.62	80.60	58.80	61.30	66.42	65.60	73.59	70.68	54.45	62.36	74.91
NVFP4-RTN-WUSH	97.07	98.00	96.12	87.32	80.82	56.25	66.60	69.26	63.90	73.26	71.06	52.54	60.72	74.84
NVFP4-RTN-I	96.50	98.50	95.74	88.49	79.57	58.71	61.25	61.05	65.75	81.22	68.48	54.78	54.87	74.22
MXFP4-GPTQ-WUSH	96.67	98.00	96.59	87.09	79.48	52.66	64.20	64.11	61.30	73.81	71.30	58.09	60.92	74.17
MXFP4-GPTQ-H	97.33	98.80	95.18	87.09	77.91	49.51	63.00	64.00	63.90	68.18	70.43	47.08	60.00	72.49
MXFP4-RTN-WUSH	97.33	97.60	96.47	85.28	76.49	52.13	59.20	65.58	61.80	70.17	70.06	50.24	57.44	72.29
MXFP4-RTN-H	94.93	97.20	92.71	83.25	73.66	45.02	59.40	60.00	63.80	69.72	65.22	50.62	57.03	70.20
	SingleOp	SingleQ	MultiArith	SVAMP	GSM8K	MMLU-Math	BBH Deduction	BBH Counting	BBH Navigate	HotpotQA	SQuAD	DROP	Winograd-WSC	Average

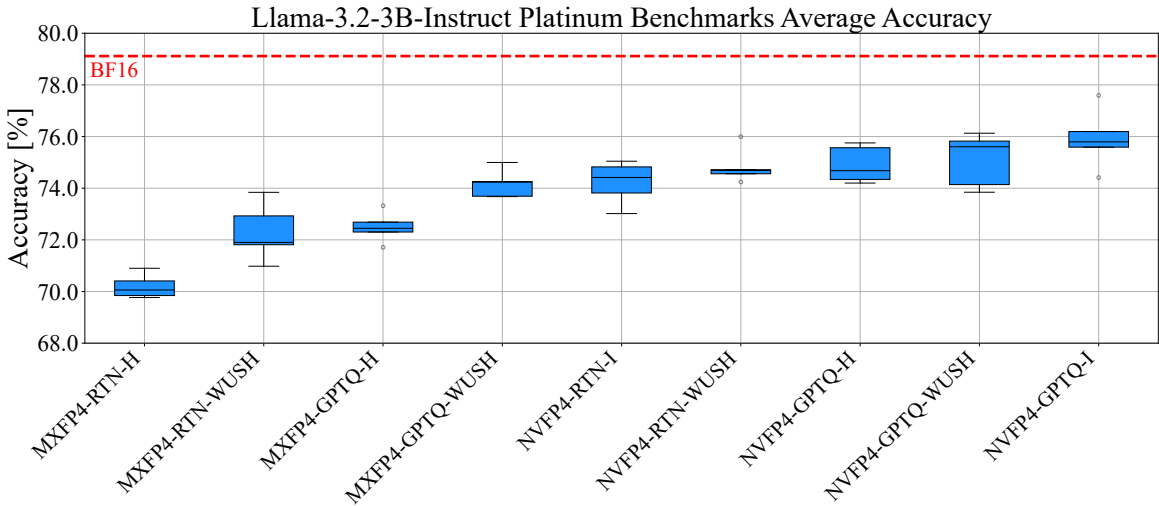


Figure 8: Comparison of different transforms on Llama-3.2-3B-Instruct for both NVFP4 and MXFP4 RTN quantization on Platinum Benchmarks. The top table shows accuracy results across the individual benchmark tasks, while the bottom plot shows the average accuracy scores together with their standard deviations for each transform.

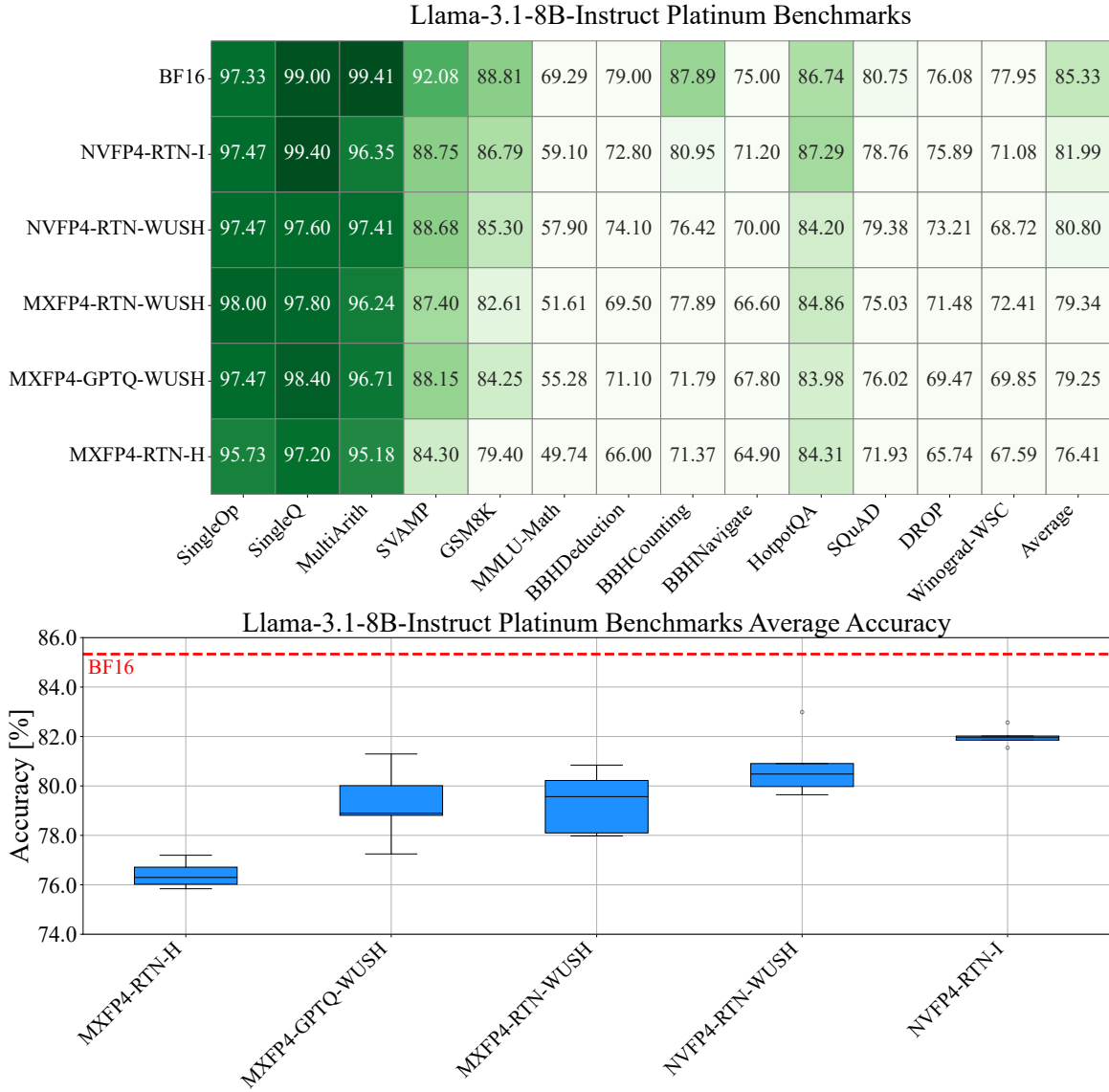


Figure 9: Comparison of different transforms on Llama-3.1-8B-Instruct for both NVFP4 and MXFP4 RTN quantization on Platinum Benchmarks. The top table shows accuracy results across the individual benchmark tasks, while the bottom plot shows the average accuracy scores together with their standard deviations for each transform.